nature communications

Article

https://doi.org/10.1038/s41467-026-74340-1

Operando identification of anion effect on lithium nucleation and growth via in situ transmission electron microscopy

Received: 30 October 2025

Accepted: 1 June 2026

Published online: 13 June 2026

Check for updates

Honglu Hu[1,10], Zhen Zhang[2,10], Mingzi Sun[3,10], So Yeon Kim[4], Se Young Kim[5], Xinru Yang[1], Liang Mei[1], Ruixin Yan[1], Weikang Zheng[1], Yue Zhang[1], M. Danny Gu[2] ✉, Guozhao Fang[6], Dongliang Chao[7], Hong-Gang Liao[8], Joon Sang Lee[5], Bolong Huang[3] ✉, Ju Li[4] ✉ & Zhiyuan Zeng[1,9] ✉

Lithium metal batteries are considered promising candidates for next-generation energy storage due to the high capacity and low redox potential of lithium negative electrodes. However, dendritic Li growth and unstable solid-electrolyte interphase formation remain critical bottlenecks for practical implementation. While electrolyte anion chemistry critically governs solid-electrolyte interphase formation, nanoscale observations of anion-regulated Li nucleation and growth mechanisms remain limited in tracking dynamic interfacial processes. Here, we employ in situ liquid-phase transmission electron microscopy combined with cryogenic spectroscopy and computational modelling to unravel anion-specific Li nucleation and growth in three distinct electrolytes: $LiClO_4$, $LiPF_6$, and LiTFSI-based electrolytes. Real-time tracking reveals that ClO_4^- drives dendritic Li growth with organic dominated solid-electrolyte interphase, whereas PF_6^- stabilizes moss-like Li nucleation through LiF-organic hybrid interphases. Notably, $TFSI^-$ forms a bilayer SEI with LiF/Li_2CO_3-rich inner layers, enabling Li lateral growth and fusion. Molecular dynamics simulations correlate anion-induced interface architectures with Li^+ transport and surface potential distributions, demonstrating that $TFSI^-$ suppresses dendrites via balanced mechanical confinement and ion-flux regulation. These anion-mediated interface engineering observations offers principles for electrolyte design toward stable lithium metal batteries.

Lithium metal batteries (LMBs) have emerged as a leading contender for next-generation energy storage technologies due to the high theoretical capacity (3860 mAh g^{-1}) and low redox potential (− 3.04 V vs. SHE) of Li metal negative electrodes[1]. Despite these intrinsic advantages, the deployment of LMBs remains hamstrung by two challenges: reactive Li dendrites and uncontrollable solid-electrolyte interphase (SEI) during cycling[2]. The electrolyte composition, particularly the choice of Li salts, plays a pivotal role in regulating SEI architecture and Li deposition behavior[3]. Among electrolyte components, anions have been recognized as key mediators in dictating SEI structure and composition through preferential decomposition pathways, which govern interfacial ion transport and Li growth behavior toward stable LMBs[4,5].

To unravel the anion-dependent mechanisms of Li deposition, studies have attempted using spectroscopic[6], electrochemical[7], and computational approaches[8]. Although advanced characterizations including in situ optical microscopy and X-ray absorption spectroscopy (XAS) provide dynamic observations[9–11], their limited spatial resolution or mixed signals from both electrolyte and electrode precludes atomic-scale insights into early-stage nucleation and interfacial

A full list of affiliations appears at the end of the paper. ✉e-mail: m.danny.gu@gmail.com; b.h@cityu.edu.hk; liju@mit.edu; zhiyzeng@cityu.edu.hk

https://doi.org/10.1038/s41467-026-74340-1

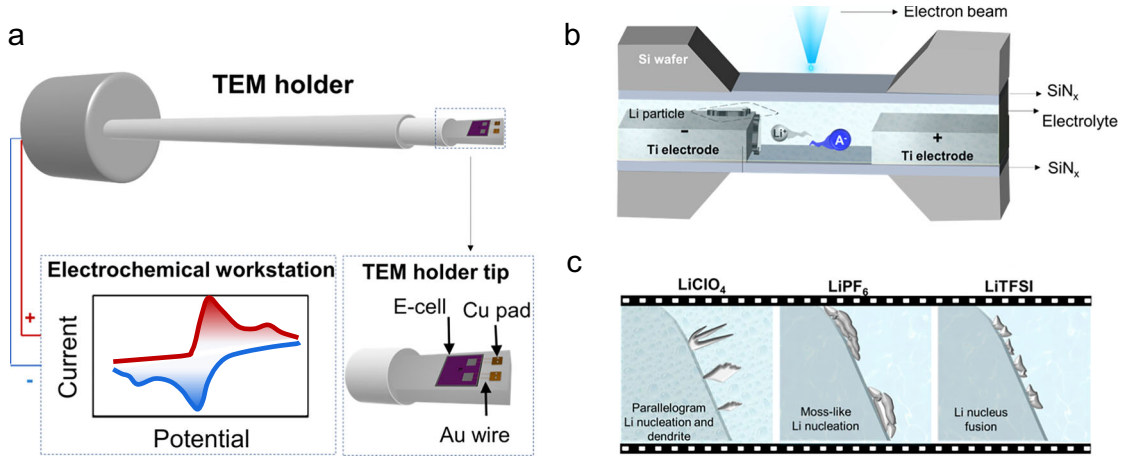

Fig. 1 | A schematic of the experimental setup for the in situ TEM study of Li initial nucleation and growth. a An electrochemical TEM sample stage and an electrochemical program is applied to the electrochemical cell using an electrochemical workstation. **b** Cross-sectional diagram of the imaging window reveals the layered structure of the liquid cell: silicon wafer, SiN_x, electrolyte, electrode, SiN_x, and silicon wafer from top to bottom. **c** In situ Li nucleation and growth on negatively charged Ti electrodes in different electrolytes.

phenomena. A critical gap persists in operando techniques capable of bridging both high spatial resolution and true electrochemical operability to directly visualize dynamic Li growth pathways under working battery conditions. In situ liquid-phase transmission electron microscopy (TEM) enables atomic or single-molecule level observation of dynamic processes with high spatiotemporal resolution[12–14]. However, limited by the thicker SiN_x observation window (~100 nm) and thick liquid layer (~1.0 μm) of the commercial liquid cell, few works have achieved the observation of the initial nucleation and growth process of Li metal under real Li-ion electrolyte conditions[15,16].

Here, we address this challenge by employing a developed high-resolution liquid-phase TEM platform with thin SiN_x imaging windows (35 nm) and liquid layer (0.15 μm), which helps to perform operando tracking of Li nucleation in three representative Li salt-based electrolytes: $LiClO_4$, $LiPF_6$, and LiTFSI (see Fig. 1, Suppl. Table S1, and Suppl. Figs. 1–3). These salts were selected as model systems due to their distinct fluorine content and bonding configurations (ClO_4^-: fluorine-free; PF_6^-: six F atoms; $TFSI^-$: six F atoms with highly anionic decomposition activity), which systematically modulate SEI composition and interfacial dynamics[17,18]. This approach enables real-time visualization of anion-regulated interfacial dynamics at nanoscale resolution under electrochemically controlled conditions. By correlating time-resolved TEM imaging with cryogenic spectroscopy, density functional theory (DFT) calculations, and molecular dynamics (MD) simulations, we establish a link between anion chemistry, SEI nanostructure, and lithium deposition morphology, offering mechanistic insights for designing anion-tailored electrolytes.

Results

Figure 1 schematically illustrates the in situ electrochemical monitoring setup using a liquid phase TEM holder. The experiment employed a 1 M $LiClO_4$ in propylene carbonate (PC) electrolyte within a sealed liquid cell integrated with patterned Ti working electrodes. Real-time Li nucleation and growth dynamics were captured during cyclic voltammetry scans (−4 to 4 V vs. Ti pseudo-reference electrode, 100 mV s^{-1} scan rate) through embedded Au wire contacts (as shown in Fig. 1a and Supplementary Fig. 1). These observations were achieved via in situ TEM imaging of electrochemical processes occurring at the SiN_x window region of the Ti working electrode (WE), revealing fundamental interfacial phenomena during lithium deposition/dissolution cycles (as shown in Fig. 1b, c).

Figure 2a presents sequential TEM snapshots capturing lithium nucleation dynamics on a Ti WE within an electrochemical liquid cell containing $LiClO_4$-PC electrolyte. The in situ TEM observations track interfacial evolution from initial Li nucleation through dendritic growth stages under a negative charge (Fig. 2d), revealing: (i) preferential lithium deposition in a parallelogram morphology (both found on the planer and the edge of Ti electrode in Fig. 2a and Suppl. Figs. 4, 5), (ii) lateral size expansion combined with anisotropic dendrite propagation (23.5 s–38.6 s) in Fig. 2e. In the capturing distinct lithium deposition pathways in a $LiClO_4$-PC electrolyte, particle 1 exhibits rapid dendritic propagation (8.5 s to 38.6 s frames), expanding laterally from 0 μm to 2.8 μm in 30 s with a growth rate of 93.3 nm s^{-1} while maintaining dendritic morphology (Fig. 2e). Particle 2 initializes as a parallelogram shaped nucleus (0.7 μm^2 projected area at t = 4.0 s, Suppl. Fig. 6) but undergoes dendritization after t = 23.5 s, achieving only 1.5 μm lateral growth despite earlier nucleation. In contrast, particle 1's transversal dimension and projected area surpasses particle 2's value by t = 23.5 s. Such preferential dendrite amplification explains Li battery failure risks, derived from self-reinforcing dendritic growth kinetics as seen in $LiClO_4$-PC electrolytes.

Figure 2b, c present sequential in situ TEM images capturing the morphology evolution of Li deposition/dissolution on Ti electrodes (Suppl. Fig. 7) in $LiPF_6$-PC electrolyte. During the discharge process (0 s to 18.5 s, Fig. 2b), three regions (area 1/2/3) consistently develop mossy Li deposits with uniform morphological features. Upon current polarity reversal at t = 18.5 s (Fig. 2f), areas 1-3 exhibit synchronized Li dissolution (Fig. 2c) with retained mossy topology until final disappearance. Notably, area 2 shows enhanced initial deposition rate (0.24 μm^2 s^{-1} vs. 0.19 μm^2 s^{-1}) and faster dissolution kinetics (−0.18 μm^2 s^{-1} versus areas 1: −0.06 μm^2 s^{-1}) over area 1 (Fig. 2g). Regardless of the variation of deposition/dissolution rates, the Li metal in all three regions maintained a flat morphology throughout the process from initial nucleation to dissolution, and no formation of dendritic structures was observed. Such mossy deposition behavior contrasts sharply with dendritic patterns observed in $LiClO_4$ electrolytes, highlighting $LiPF_6$'s optimized kinetics for stable Li cycling in practical cells.

Figure 3a–c reveals the morphology evolution of lithium deposition/dissolution on Ti electrodes with applied electric field in LiTFSI-PC electrolyte. The sequential TEM frames in Fig. 3a demonstrate Li growth with terrace-like nucleation (stage 1 in Fig. 3d) progressing to lateral coalescence of adjacent nuclei (stage 3 in Fig. 3d) (103–115 s, the full video and electrochemical curve shown in Supplementary Video 3 and Suppl. Fig. 8). Stage 3 exhibits planar cross-growth (red arrows) devoid of dendrites, maintaining sub-400 nm flat lithium deposition. Under a positive current, the lithium particles completely dissolved

https://doi.org/10.1038/s41467-026-74340-1

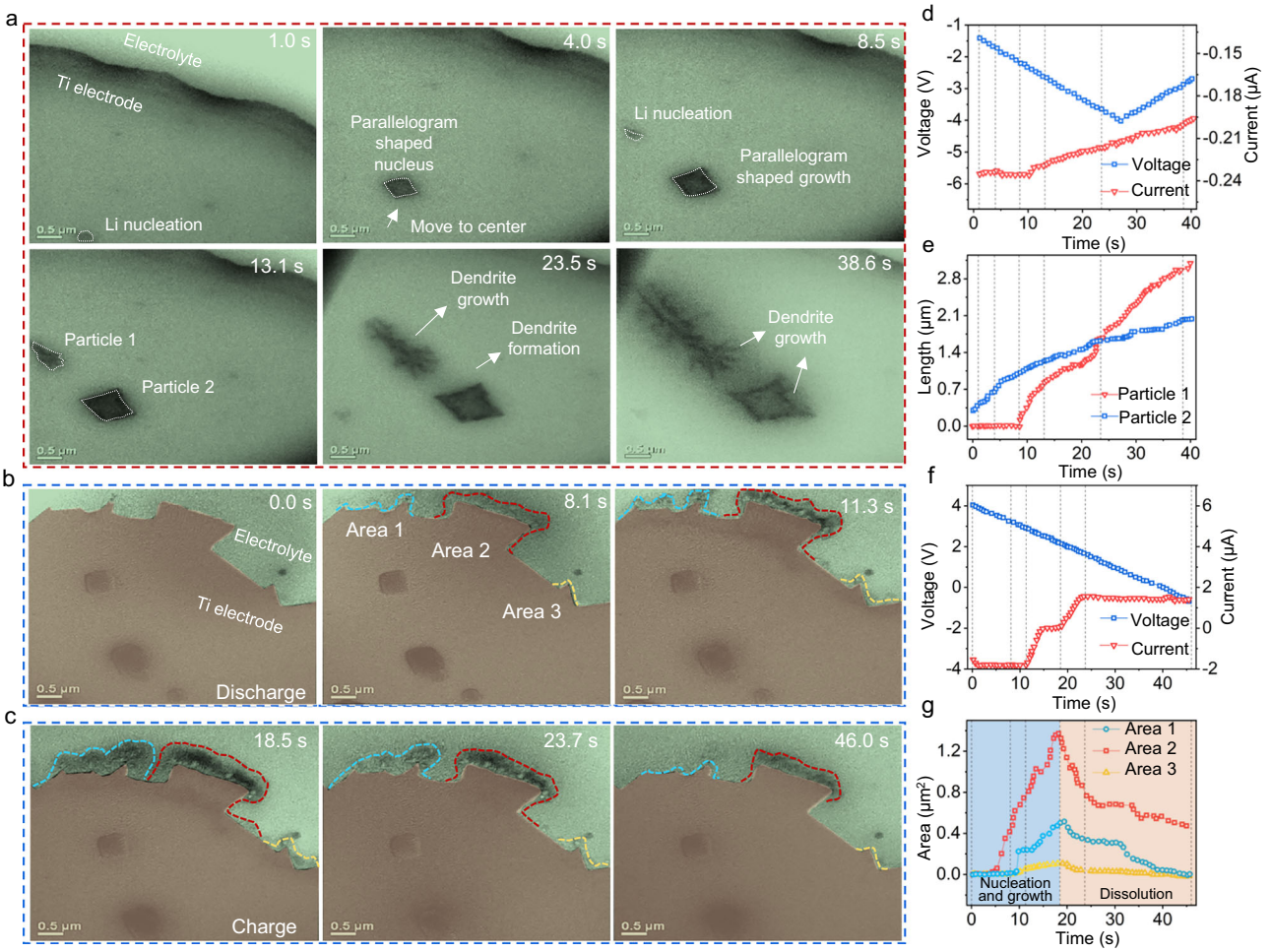

Fig. 2 | Morphology evolution of Li nucleation on Ti electrode in $LiClO_4$-PC and $LiPF_6$-PC electrolyte. a Time-series TEM images from Supplementary Video 1 of Li nucleation and growth on Ti electrode in an electrochemical liquid cell. Scale bars, 500 nm. **b**, **c** Time-series TEM images from Supplementary Video 2 of Li nucleation, growth (**b**) and dissolution (**c**) on Ti electrode (dashed red frame) in an electrochemical liquid cell. **d**, **e** The applied electric field (**d**), the corresponding transversal dimensions (**e**) variation as a function of time for particles 1 and 2. **f**, **g** The applied electric field (**f**) and the corresponding projection area (**g**) variation as a function of time for areas 1, 2, and 3. Electrochemical tests were conducted at 20 °C, and cycling current are shown in (**d**, **f**). Source data are provided as a Source Data file.

and vanished at 127 s (the projected areas dropped to zero within the 8 s interval, Fig. 3b), leaving no residual irreversible lithium dendritic structures. Figure 3d illustrates the 3D reconstructed Li coverage—(1) nucleation, (2) cross growth, (3) fusion, (4) planar expansion, (5) dissolution onset, (6) complete dissolution, validating LiTFSI's efficacy in sustaining dendrite-free and reversible Li deposition/dissolution.

Cryogenic transmission electron microscopy (cryo-TEM) was employed to analyze the SEI formed at Li-electrolyte interfaces in three representative electrolytes: $LiClO_4$-PC, $LiPF_6$-PC, and LiTFSI-PC. Scanning electron microscope (SEM) and low-magnification cryo-TEM images for deposited Li on TEM copper meshes (Suppl. Fig. 9) revealed distinct SEI (Supplementary Fig. 10a–c) morphologies across these electrolytes. High-resolution imaging demonstrated that $LiClO_4$-PC electrolyte generated a ~ 23.1 nm thick SEI containing few randomly dispersed crystalline nanoparticles (5–10 nm diameter, marked by red line) within an amorphous matrix, identified as Li_2CO_3 through lattice matching (Fig. 4a). A similar organic-inorganic hybrid structure was observed in $LiPF_6$-PC electrolyte, though with additional LiF and Li_2O crystalline components characteristic of PF_6^--derived mosaic-structured SEIs (Fig. 4b).

In contrast, LiTFSI-PC electrolyte produced a layered SEI (~ 25.9 nm thick) comprising an outer amorphous organic layer (~ 5 nm) and an inner inorganic-rich region (~ 20 nm) containing LiF/Li_2CO_3 crystallites (Fig. 4c). Cryogenic electron energy loss spectroscopy (cryo-EELS) confirmed these compositional differences: both $LiPF_6$-PC and LiTFSI-PC systems exhibited Li_2CO_3 signatures in Li/O K-edges, while LiTFSI-PC showed stronger F K-edge intensity indicative of higher LiF content (Fig. 4d, e). The $TFSI^-$-derived SEI displayed enhanced C-H/C-O σ* transitions in C K-edge spectra, consistent with organic-rich surface layers[19]. These structural and compositional variations highlight the critical role of anion chemistry in determining SEI architecture.

Cryogenic scanning transmission electron microscopy (cryo-STEM) combined with EELS-mapping revealed the spatial distribution of key elements (Li, C, O, F) at the Li/electrolyte interface. In $LiPF_6$-PC electrolyte, all elements exhibited uniform dispersion within the amorphous SEI matrix without obvious phase segregation after three charging /discharging cycles (Fig. 4f) and thirty charging/discharging cycles (Suppl. Fig. 11). Analysis of element overlay profiles demonstrated mixed spatial distributions of F and O components relative to bulk Li metal (Fig. 4f), suggesting homogeneous embedding of inorganic species (e.g., LiF) within the organic SEI framework. This amorphous SEI with mosaic-structured inorganic components maintains structural stability during lithium deposition, exhibiting enhanced mechanical integrity and flexibility. As evidenced by the synchronized dissolution kinetics in Fig. 3a, b, the $LiPF_6$-derived self-limiting SEI

https://doi.org/10.1038/s41467-026-74340-1

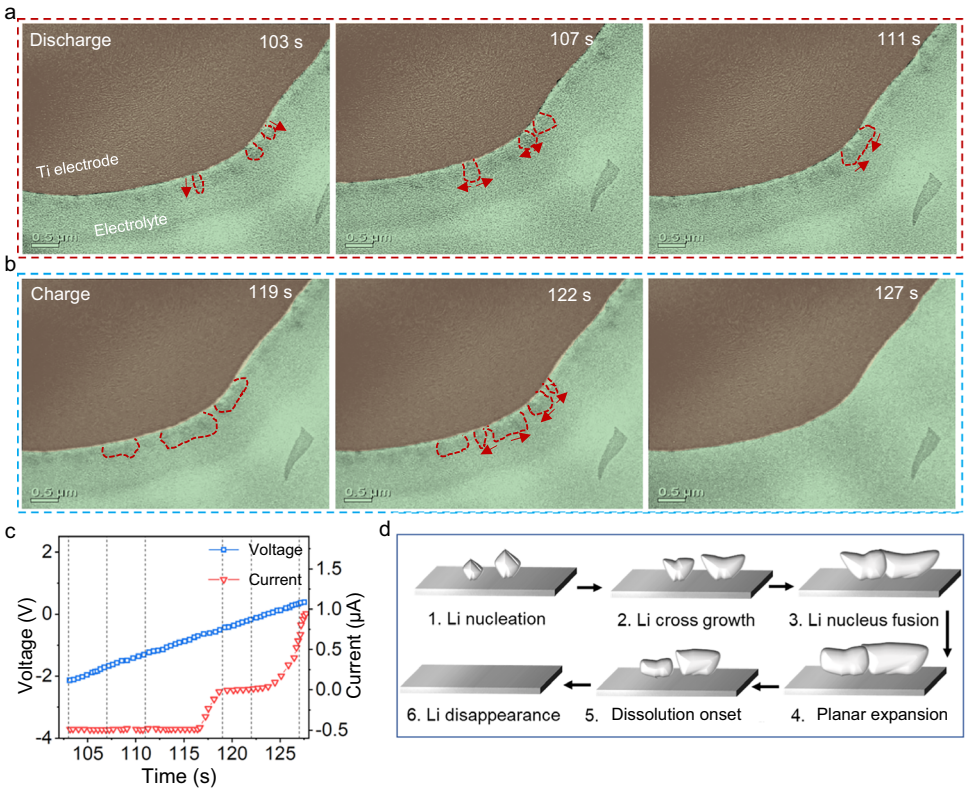

Fig. 3 | Morphology evolution of Li nucleation and growth in LiTFSI-PC electrolyte. a, **b** Time-series TEM images from Supplementary Video 3 of Li deposition (**a**) and dissolution (**b**) in the liquid cell. The red arrows indicate the directions of growth of Li. **c** Temporal evolution of the applied electric field. **d** 3D images corresponding to (**a**, **b**) display the behavior of Li nanoparticles. Electrochemical tests were conducted at 20 °C, and cycling current are shown in (**c**). Source data are provided as a Source Data file.

formation effectively restricts dendrite initiation through its LiF-organic hybrid interphase.

In contrast, the LiTFSI-PC electrolyte exhibited persistent elemental stratification across cycling stages: fluorine signals consistently concentrated near the inner SEI layer while oxygen maintained uniform spatial distribution throughout the SEI thickness, as evidenced by both 3-cycle (Fig. 4g) and 30-cycle (Suppl. Fig. 12) characterizations. This configuration reveals an organic/inorganic hybrid architecture with an outer flexible organic-rich layer and inner rigid inorganic-rich phase, aligning with a "flexible outer-robust inner" design principle for optimized SEI stability. The inorganic-dominated inner layer enhances ionic conductivity and mechanical strength, while the outer organic phase accommodates volume changes during cycling, synergistically improving interfacial compatibility and structural durability[20].

We characterized the composition and structure of the SEI using in-depth etching X-ray photoelectron spectroscopy (XPS), focusing on representative $LiPF_6$-PC and LiTFSI-PC electrolytes. The Li 1 s, O 1 s, and F 1 s spectra of the SEI on lithium metal were analyzed at different sputtering times (0–65 s) in $LiPF_6$- and LiTFSI-based electrolytes (Fig. 5a, b). In the $LiPF_6$-PC electrolyte, the characteristic peaks corresponding to LiF (684.8 eV) and Li_2CO_3 (682.0 eV) exhibited consistent intensity profiles across the SEI layers, from the outer surface to the inner regions adjacent to the bulk Li metal, while Li_2O peaks (528.1 eV) gradually increased with sputtering depth (Fig. 5a). In contrast, the LiTFSI-PC electrolyte exhibited distinct behavior: the C-F peak at 688.6 eV (attributed to -CF_3 species from residual LiTFSI) diminished progressively with sputtering time and eventually disappeared (Fig. 5b). The LiF content gradually increased in the inner SEI layers, which matched the fluorine-rich regions identified through cryo-STEM EELS mapping. This observation aligns with the cryo-TEM results, confirming the depth-dependent compositional evolution in SEI. Quantitative analysis of SEI composition demonstrated that the relative proportion of LiF within the interphase structure of LiTFSI-PC progressively exceeded that observed in $LiPF_6$-based electrolyte with increasing sputtering depth (Fig. 5c). These findings demonstrate that LiTFSI-derived SEI features a fluorine-rich inner layer, while $LiPF_6$ generates a more homogeneous distribution of LiF components. Large-area elemental mapping from SEM revealed that the LiTFSI-derived electrolyte facilitates the formation of a fluorine-enriched SEI (Supplementary Fig. 13), as manifested by its significantly higher fluorine content (9.3 wt.%) compared to $LiPF_6$-based systems (3.7 wt.%).

To understand the influences of the anions in the Li salts on the formation of Li dendrite and SEI, we have carried out integrated research combining both DFT calculations and MD simulations to explore the interactions between electrolyte and Li surfaces. First of all, we compare the adsorption energies of different electrolyte molecules on the Li surface (Fig. 5d). We notice that all the molecules show strong adsorption trends on the Li surface with negative binding energies. $LiClO_4$ maintains structural configurations after adsorption without the dissociation of O-Cl bonds. In comparison, both $LiPF_6$ and LiTFSI have revealed evident bond dissociation for P-F and C-F bonds, where the free F atoms are able to combine with free Li ions to form LiF. This leads to the high concentration of LiF in the SEI structure for Li electrodes with $LiPF_6$ and LiTFSI electrolytes. For the PC, the original five-member ring structure is damaged owing to the interactions with the Li surface, which is the key reason for the organic components in the SEI.

The analysis of the highest occupied molecular orbitals (HOMO) and lowest unoccupied molecular orbitals (LUMO) of different electrolyte anions indicates that $TFSI^-$ with the lowest LUMO position supports the strongest possibility to accept electrons and undergo the reduction

https://doi.org/10.1038/s41467-026-74340-1

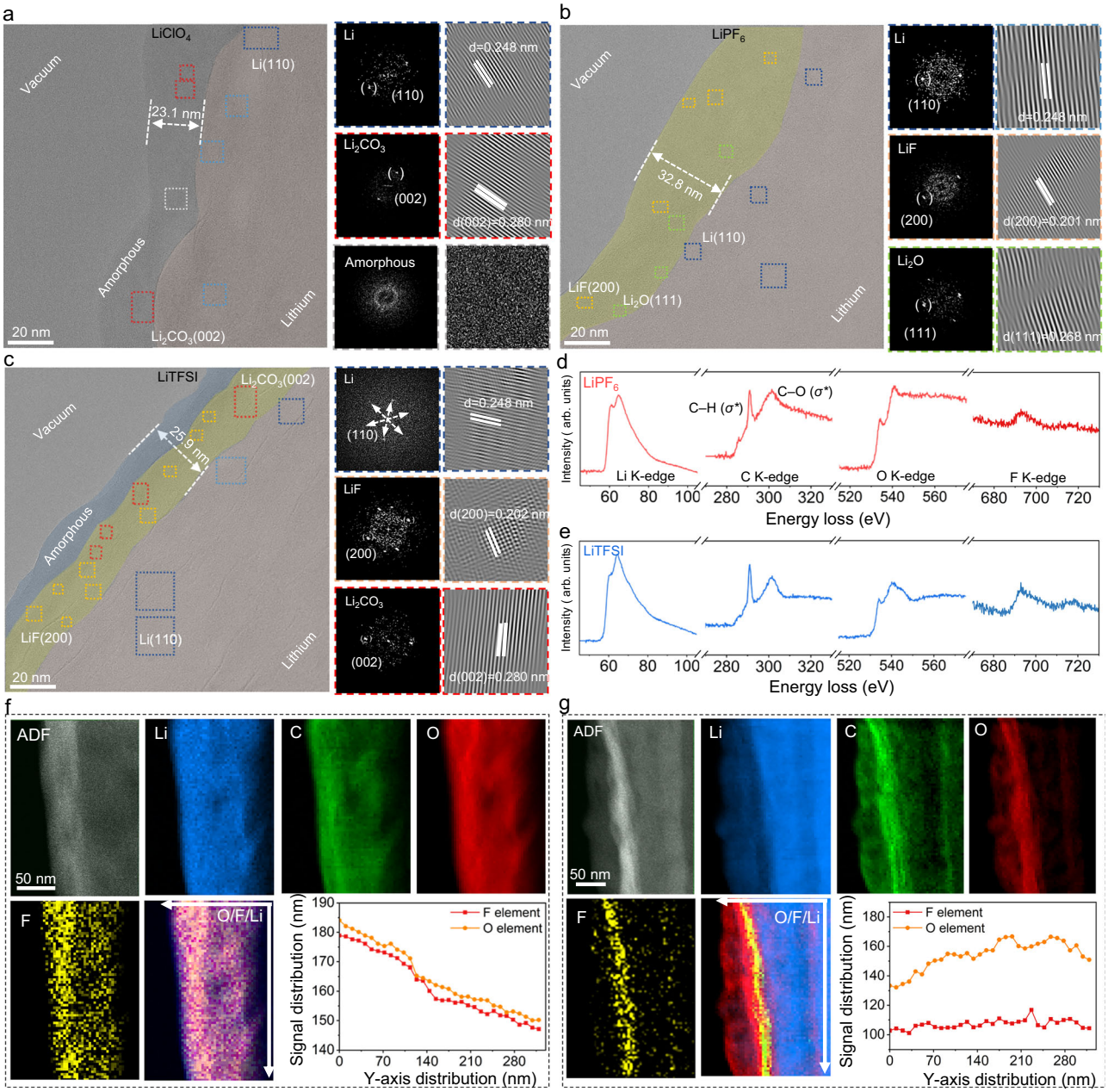

Fig. 4 | Microstructure of the SEI formed in electrolytes of various Li salts after three charging/discharging cycles. a–c Cryo-TEM images of SEI on deposited Li metal and selected components with corresponding fast Fourier transform pattern in $LiClO_4$ (**a**), $LiPF_6$ (**b**) and LiTFSI-based (**c**) electrolytes. **d**, **e** Cryo-TEM/EELS analysis of SEI on deposited Li in $LiPF_6$ (**d**) and LiTFSI (**e**) electrolytes. **f**, **g** Cryo-STEM ADF images, EELS mapping images and element overlay profiles for distributions of F and O elements on Li metal surface in the $LiPF_6$ (**f**) and LiTFSI-based (**g**) electrolytes. All the batteries for cryo-TEM tests were in a fully discharged state after 3-cycle cycling at 20 °C with a current density of 2.0 mA cm^{-2} and a capacity density of 1.0 mAh cm^{-2}. Source data are provided as a Source Data file.

process towards decompositions (Supplementary Fig. 14a). Moreover, different anions also result in varying solvation structures in the electrolyte, where the radial distribution function (RDF) reveals that $TFSI^-$ anions show the weakest solvation capability, and are mostly exposed on the Li surface, resulting in the decompositions (Supplementary Fig. 14b–d). In comparison, the ClO_4^- anions display the strongest trend to be involved in the Li solvation structure. This further limits the contact of ClO_4^- anions with the electrode surface, explaining the limited dissociation of ClO_4^-. Moreover, the calculated bond dissociation energies reveal that the S-N bond (1.8 eV) is significantly weaker than the C-F bond (3.4 eV), indicating preferential S-N cleavage during the initial reduction of $TFSI^-$. Such early-stage decomposition generates organic and sulfur-containing fragments, contributing to the formation of the outer organic-rich SEI layer. In contrast, the higher C-F bond dissociation energy suggests that C-F cleavage requires stronger reducing conditions, which are primarily available near the electrode surface. This leads to LiF formation predominantly in the inner SEI region, consistent with experimental observations.

To observe the interactions of the Li surface with electrolyte molecules, we demonstrate the interaction energies (Suppl. Fig. 15). After the introduction of PC on the surface, the interaction energy of $LiClO_4$ has been significantly reduced due to the decomposition of PC, resulting in the high organic components in the SEI of the $LiClO_4$ electrolyte. Similarly, the PC introduction lower interaction energies for $LiPF_6$ and LiTFSI electrolytes, which is mainly contributed by the strong dissociation of P-F and C-F bonds, further supporting the

https://doi.org/10.1038/s41467-026-74340-1

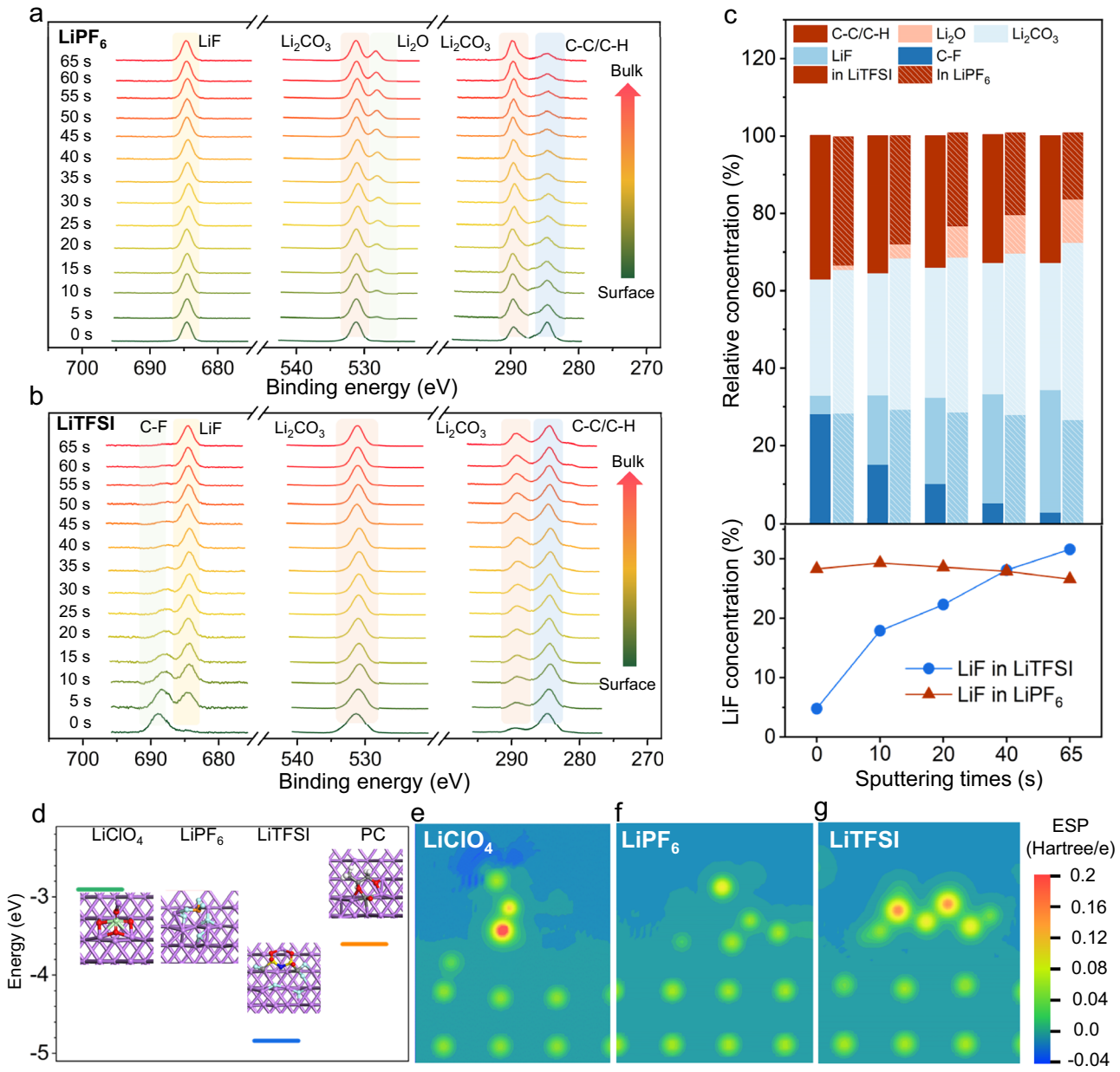

Fig. 5 | Component analysis of the SEI formed on Li metal in different electrolytes. a, **b** XPS of Li 1 s, O 1 s, and F 1 s spectra of SEI on Li metal at different sputtering times (0–65 s) in the $LiPF_6$ (**a**) and LiTFSI (**b**) electrolytes. **c** Quantitative analysis of the relative abundances of decomposition products within the SEI. All the batteries for XPS tests were in a fully discharged state after 3-cycle cycling at 20 °C with a current density of 2.0 mA cm^{-2} and a capacity density of 1.0 mAh cm^{-2}. **d** The adsorption energies and structural configurations of different electrolyte molecules on the Li surface. Purple balls = Li, green balls = Cl, orange balls = P, light blue balls = F, yellow balls = S, blue balls = N, red balls = O, green balls = C, and white balls = H. **e**–**g** The electrostatic potential of Li surface with different electrolytes of $LiClO_4$ (**e**), $LiPF_6$ (**f**), and LiTFSI (**g**). Source data are provided as a Source Data file.

formation of LiF in the SEI. Then, we investigate the electronic structure changes of surface Li sites after the adsorptions of electrolyte molecules (Suppl. Fig. 16). Compared to the pristine Li surface, the 2 s orbitals have been modulated, confirming the electron transfer between the Li surface and electrolyte molecules during the interactions. Such strong interactions play a key role in the formation of SEI on the Li surface. Besides the Li sites, the s, p orbitals of electrolyte molecules are also compared before and after interactions with Li surfaces (Suppl. Fig. 17). The p orbitals in $LiClO_4$ have shown dominant contributions near the Fermi level (E_F) while the s orbitals are located far from the E_F. After interactions with Li surfaces, the electronic structures evidently downshifted for both s and p orbitals, which is attributed to the electronic modulations induced due to the distortion of $LiClO_4$. For $LiPF_6$, it is noted that the electronic structures not only downshift but also display evident changes, which are ascribed to the decomposition of $LiPF_6$ with electron transfer from the Li surface, facilitating the generation of LiF (Suppl. Fig. 18). Similarly, the LiTFSI also exhibits significant structure decompositions, which results in the dramatic change of the PDOSs, indicating strong interactions with the Li surface (Suppl. Fig. 19). In particular, the s orbitals become much flattened, and the gap between the valence band maximum (VBM) and conduction band minimum (CBM) has been largely reduced. Then, for the PDOS of PC, the $LiClO_4$ electrolyte has shown slightly stronger downshifting and modulations, which potentially causes more decomposition of PC to induce high organic compositions in the SEI phase (Suppl. Fig. 20).

To further investigate the Li deposition trend with different electrolytes, we have demonstrated the surface potential modulations of Li surfaces. For the $LiClO_4$ electrolyte, the high uneven surface potential is observed, especially the ClO_4^- anions cause the inhomogenous tip-like potential distributions on the Li surface (Fig. 5e). Such a surface is highly possible to induce the formation of Li dendrite following the inhomogeneous potentials. In comparison, the surface potential of Li surface in $LiPF_6$ electrolyte becomes much even, which benefits the deposition of Li in the horizontal directions, leading to moss-like nucleation (Fig. 5f). Although the LiTFSI also induces an uneven potential distribution, it is much more flattened than that of the $LiClO_4$ electrolyte (Fig. 5g). Under such a potential distribution, the Li depositions initially form small Li nuclei by growth in the vertical direction. Then, the small nuclei will start to grow in the horizontal direction, which then causes nuclei fusions. The Li diffusion barriers on the Li surface also reveal that the $LiClO_4$ electrolyte displays the highest barriers, which limit the horizontal growth of Li and facilitate the dendrite formation (Suppl. Fig. 21).

While the macroscopic electric field naturally concentrates at the electrode edges (promoting edge-preferential growth, as predominantly observed in the uniform $LiPF_6$-PC system), the SEI formed in the $LiClO_4$-PC electrolyte induces severe localized potential fluctuations. These microscopic hotspots trigger chaotic nucleation across the entire electrode. Consequently, in the $LiClO_4$-PC system, severe dendritic growth is observed not only on the flat top surface (as shown in Fig. 2a) but also at the electrode edges (Suppl. Fig. 5 and Suppl. Video 5).

Both $LiPF_6$ and LiTFSI electrolytes have decreased diffusion barriers for Li, which benefits the horizontal growth of Li. Since the $LiPF_6$ electrolyte exhibits a slightly lower energy barrier for Li diffusion than LiTFSI, the Li nucleus potentially shows a faster growth speed than that of the LiTFSI. After the SEI is fully formed, Li^+ deposition no longer occurs directly on the bare Li surface, but is dominated by the ESP distribution of the SEI, where both LiF (001) and Li_2CO_3 (001) surface exhibits a highly uniform electrostatic potential distribution (Supplementary Fig. 22a, b, d, e). These results explain that the PF_6^- system can effectively homogenize the interfacial electric field, suppress the tip effect, and induce uniform moss-like Li deposition. The good potential energy level matching between LiF (001) and Li_2CO_3 (001) facilitates the continuous inorganic inner layer formation for the LiTFSI electrolyte, which effectively inhibits local enrichment of Li^+ flux and continuously supports the lateral growth and fusion of Li nuclei in later growth stages towards dendrite-free deposition. In comparison, the amorphous organic phase in $LiClO_4$-derived SEI shows evident local potential fluctuations due to the lack of long-range ordered bonding and uneven charge distribution, leading to an inhomogeneous overall potential distribution. This continuously induces local Li^+ enrichment and vertical dendritic propagation (Suppl. Fig. 22c, f).

To experimentally validate the kinetic advantages predicted by our computational models, Tafel plot measurements were performed to quantify the exchange current density (i_0) across different SEIs (Suppl. Fig. 23). The calculated i_0 values display a clear trend: $LiClO_4$ (0.019 mA cm^{-2}) < $LiPF_6$ (0.045 mA cm^{-2}) < LiTFSI (0.079 mA cm^{-2}). The highest i_0 in the LiTFSI-based electrolyte indicates highly facile interfacial charge-transfer kinetics, corroborating the low diffusion barrier derived from our DFT calculations.

To evaluate the relationship between in situ observations and macroscopic battery performance, we conducted electrochemical cycling tests using standard coin cells (Suppl. Figs. 24 and 25). In Li||Li symmetric cells, the LiTFSI-PC electrolyte supported stable cycling for over 500 hours with an overpotential of ~125 mV, corresponding to the lateral growth mechanism that reduces the risk of dendrite-induced short circuits. Conversely, the $LiClO_4$-PC cells exhibited short-circuiting within 240 hours, consistent with the observed dendritic growth. In Li||Cu half-cell tests, the LiTFSI-PC cells demonstrated an average Coulombic efficiency (CE) of 91.6%, compared to 37.8% for the $LiClO_4$-PC cells. Although the absolute CE values are limited by the inherent reactivity of the PC solvent with lithium metal, the comparative data indicate that the SEIs induced by $TFSI^-$ more effectively mitigates irreversible active lithium loss. Overall, these macroscopic electrochemical evaluations align with the anion-regulated morphological evolutions observed at the nanoscale.

In addition, we have also carried out the MD simulations of different electrolytes. After MD simulations, we notice that most of the PC molecules in the $LiClO_4$ electrolyte are decomposed into different types of carbon chains or small organic fragments, supporting the organic-rich SEI phase (Suppl. Fig. 26a, b). The Li surface becomes highly distorted, and the Li atoms mainly diffuse in the vertical direction, which promotes the formation of Li dendrite. In contrast, the surface Li atoms are less distorted in the $LiPF_6$ electrolyte with reduced diffusions in the vertical direction (Suppl. Fig. 26c, d). Moreover, the preservation of PC molecules and the formation of LiF are noted, indicating the LiF-rich structures in the SEI phase. For the LiTFSI electrolyte, we have noticed not only the decomposition of LiTFSI but also the formation of LiF (Suppl. Fig. 26e, f). The formation of Li_2CO_3 near the Li surfaces is also noted, which is induced by the decomposition of PC in the electrolyte.

To evaluate the migrations of Li and the possibility for dendrite formation, the MD simulations are further compared in an enlarged $10 \times 10 \times 10$ supercell of Li surface regarding the interaction with Li salt and PC (Suppl. Figs. 27, 28). As shown in Supplementary Fig. 27, the diffusions of Li atoms form the uneven surface with evident concave and convex induced by the Li deposition, where the convex part of the Li deposition potentially becomes the Li nuclei and facilitates the Li dendrite formation. In comparison, the deposition of Li in LiTFSI surfaces is most even when compared to $LiClO_4$, where only a minor convex region is noted (Suppl. Fig. 28). The most even deposition of Li in LiTFSI electrolyte results in the relatively weak Li dendrite formation. For the MD simulations, Li diffusion behaviors are most active in LiTFSI while the $LiClO_4$ electrolyte exhibits slower migration (Suppl. Fig. 29). From these results, LiTFSI is able to guarantee ionic conductivity without causing a strong formation of Li dendrite.

Figure 6 schematically illustrates the Li salt-type-dependent regulation of Li deposition morphology through anion-mediated SEI engineering. In $LiClO_4$ systems (Fig. 6a), strong PC decomposition and preserved O-Cl bonding create organic-rich, insufficient inorganic phases and mechanically weak SEI layers. The resultant high Li diffusion barriers and tip-enhanced surface potential promote vertical dendrite growth. While initial nucleation demonstrates relatively uniform morphology, subsequent Li deposition undergoes uncontrolled longitudinal propagation, ultimately evolving into dendritic structures due to insufficient interfacial stabilization.

In contrast, $LiPF_6$-derived electrolytes facilitate the formation of hybrid SEI architectures with homogeneously dispersed LiF nanocrystals embedded in organic matrices (Fig. 6b). This hybrid material combines inorganic and organic components to strengthen the structure while keeping the interface flexible. Together, these features help lithium form dense, moss-like deposits during controlled electroplating. The synergistic interplay between inorganic reinforcement and organic elasticity effectively suppresses dendrite penetration without compromising ionic transport.

Notably, LiTFSI-based electrolytes form a bilayer SEI structure with complementary functional layers (Fig. 6c). Specifically, our observation suggests the following scenario. As soon as metallic Li (Li_{Metal}; atomic structure in the early stages may not yet adopt the body-centered arrangement Li_{BCC}) forms, it reacts with dissociation products to form inorganic phases. The thermodynamic driving force for this reaction lowers the effective wetting angle of Li_{Metal}, promoting "reactive wetting"[21]. Consequently, Li_{Metal} creeps laterally over the surface of the current collector at the nanometer scale, increasing true

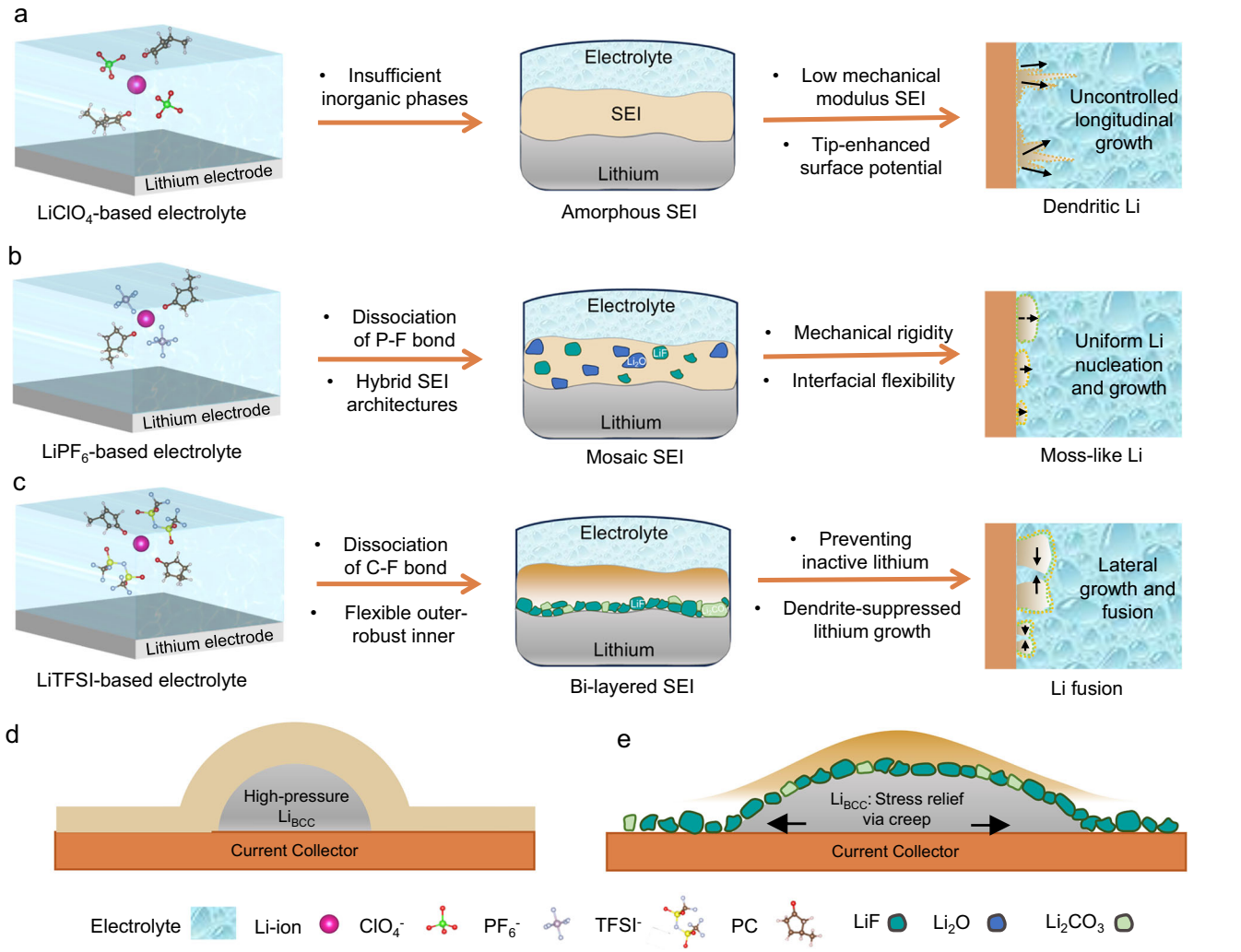

Fig. 6 | The schematic of anion effect on SEI formation and Li growth process in. a $LiClO_4$, (**b**) $LiPF_6$, and (**c**) LiTFSI electrolytes. The schematic of (**d**) organic SEI and (**e**) organic/inorganic bilayer SEI for Li deposition.

contact area for Li_{BCC} deposition. Depending on how wettable these inorganic phases are by the organic-rich SEIs, the SEI may form either an intermixed or a distinct bilayer. The inorganic SEI is less resistive to Li^+ transport, and its interface with Li_{BCC} can potentially act as an artificial mixed ionic/electronic conductor[22] with high Li^0 diffusivity. This enables separately formed Li_{BCC} (i.e., metallic Li with body-centered cubic structure[23]) islands, initially covered by inorganic SEI, to fuse via metallic Li flow at the inorganic SEI/Li_{BCC} interface and the SEI/current collector interface when two islands became in contact.

In contrast, the organic-rich region is more resistive to Li^+ transport and thus increases electrochemical impedance[24], which can build mechanical pressure within underlying Li_{BCC} deposits. Under an overpotential of just a few tens of millivolts, the resulting hydrostatic pressure can theoretically reach sub-gigapascal levels (per the Nernst equation) if not relieved quickly through Li_{BCC} creep[25]. While Li_{BCC} creep is sluggish in other electrolytes (leading to greater stress accumulation; Fig. 6d), the inorganic-rich inner layer derived from a LiTFSI-type anion may support faster Li_{BCC} creep, mitigating stress buildup (Fig. 6e) and preventing abrupt fracturing of the organic layer. Nonetheless, the organic layer may still thicken and become so resistive that Li_{BCC} deposition temporarily halts locally until stress becomes immense. At that point, the organic layer may fracture abruptly—often at its thinnest region near the top of the SEI—leading to Li deposition there and promoting dendritic Li growth.

The inner inorganic-rich rigid layer adjacent to Li metal comprises continuous LiF phases that establish mechanical stability, while the outer flexible organic-dominated layer interfaces with the electrolyte to maintain interfacial adaptability. This dual-layer structure acts as a protective interface with two key functions. The strong LiF inner layer physically restricts lithium deposition patterns through its rigid framework, effectively blocking the buildup of inactive lithium. Meanwhile, the flexible outer layer rich in organic components allows smooth Li growth across the surface during repeated charging-discharging cycles, preventing dendrite formation while maintaining a stable interface between the Li metal and electrolyte. This structural evolution highlights how salt anion chemistry governs interfacial stability through coordinated mechanical and chemical effects, where the outer compliant layer accommodates electrolyte interactions while the inner rigid layer stabilizes Li metal contact. The distinct functional roles of the "flexible outer-rigid inner" bilayer SEI (Fig. 6) can be justified by the intrinsic mechanical properties of its specific chemical components (Suppl. Table S2). The inner layer, predominantly enriched with inorganic components such as LiF, Li_2CO_3, and Li_2O, acts as a mechanically robust barrier with Young's moduli (E) typically up to 45 GPa. This "rigid" inner layer provides the structural stiffness necessary to physically block dendrite penetration. Conversely, the outer layer is dominated by organic oligomers and alkyl carbonates, which intrinsically exhibit low Young's moduli ($E < 5.0$ GPa). This low-

modulus composition imparts substantial mechanical compliance to the outer layer, allowing it to act as a "flexible" cushion.

Our operando investigation unveils fundamental anion-dependent mechanisms governing lithium nucleation and morphology evolution through correlative in situ TEM imaging, cryogenic spectroscopy, and computational simulations. These atomic-scale insights establish a mechanistic paradigm for anion-mediated SEI engineering: optimal anions must balance two criteria: (i) forming a rigid inorganic-rich underlayer (e.g., continuous LiF phases) to physically restrict Li deposition morphology and promote lateral Li creep for stress mitigation, (ii) maintaining an organic-dominated flexible overlayer to accommodate interfacial dynamics while avoiding excessive impedance buildup. Our findings highlight anion chemistry as a critical factor for interfacial control, where coordinated SEI components type and distribution collectively dictate lithium morphology, providing guidelines for next-generation Li-metal battery developments.

Methods

Materials

Lithium perchlorate ($LiClO_4$, 99.9%, DodoChem Technology Co., Ltd), Lithium hexafluorophosphate ($LiPF_6$, 99.9%, DodoChem Technology Co., Ltd), Lithium bis(trifluoromethane)sulfonimide (LiTFSI, 99.9%, DodoChem Technology Co., Ltd), Propylene carbonate (PC, 99.9%, DodoChem Technology Co., Ltd), Dimethyl carbonate(99%, Sigma-Aldrich), Ethanol (99%, Aladdin), Li foils (99.9%, Sigma-Aldrich), Copper foil (99.9%, Shenzhen Kejing Electronic Technology Co., Ltd.). The deionized (DI) water was purified using Milli-Q System.

Fabrication of electrochemical liquid cell

The electrochemical liquid cell was constructed with key structural components comprising paired silicon chips. Thin p-doped silicon wafers (200 μm thickness, Virginia Semiconductor) served as substrates. A critical 35 nm low-stress silicon nitride membrane was deposited via vapor growth to enable electron-transparent observation. The bottom and top chips were patterned through photolithography and subsequently etched in KOH solution to create viewing windows (25 × 6 μm dimensions) flanked by dual reservoirs. The spatial resolution and signal-to-noise ratio (SNR) in LP-TEM are governed by the thicknesses of the SiN_x imaging windows and the liquid spacer. Our design utilizes 35 nm SiN_x windows and a ~150 nm liquid spacer. This configuration reduces the total electron penetration thickness to ~220 nm, substantially minimizing background scattering and translating into high SNR. To provide a broader context of recent technological progress in the field, a comparison of our custom cell configuration with a wider range of recent representative LP-TEM studies is summarized in Suppl. Table S3.

Electrode architecture was implemented through physical vapor deposition of 90 nm titanium layers on bottom chips, forming face-to-face working/counter electrode pairs with 20 μm interelectrode spacing. Device integration involved precision alignment of top/bottom chips using a 150 nm sputtered indium interlayer as spacer and then sealed with hermetic sealant. Electrolyte infusion was conducted under inert atmosphere, where 1 M lithium salts (e.g., $LiClO_4$, $LiPF_6$, or LiTFSI) in propylene carbonate solvent were syringe-injected into reservoirs, achieving capillary-driven fluidic filling of the observation chamber (final device dimensions: 3 × 3 × 0.4 mm^3).

For in situ TEM biasing, the microcell was integrated into a customized holder (JEOL 2100 compatible) through wire bonding-aluminum interconnects bridged titanium contact pads to copper terminal blocks. A two-electrode configuration was implemented by functional differentiation of deposited Ti structures into working and counter(reference) electrodes through cleanroom-assembled circuitry. This architecture enabled real-time electrochemical characterization under controlled potential conditions during TEM observation.

Material characterizations

Real-time monitoring of dynamic electrochemical process was conducted with transmission electron microscopy (JEOL 2100, 200 kV acceleration voltage) equipped with a Gatan Orius CCD camera for high-resolution imaging. SEM (JEOL JSM-7600F) was employed to analyze morphological evolution during electrochemical processing. As for preparation of ex-situ measurements of the electrode samples, all batteries were first disassembled in an Ar-filled glove box. The electrodes were immersed in DMC solvent (water content < 30 ppm) for 30 min, then rinsed three times with DMC and dried in the glove box, stored for subsequent tests at 20 °C (± 2 °C). For cryo-EM characterizations, a stringent cryogenic transfer protocol was employed to preserve the native state of the beam-sensitive interphases. Inside the glovebox, the sample-loaded TEM grids were placed into Ar-filled glass vials and sealed within a triple-layer protective container to maintain an absolute Argon micro-atmosphere. The assembly was then rapidly plunged into liquid nitrogen. This plunge-freezing process immobilizes the local chemical environment, preventing any room-temperature structural evolution or component redistribution. The grids were subsequently transferred into the microscope via a cryogenic auto-loader, ensuring continuous maintenance under high vacuum. Furthermore, to prevent electron-beam-induced structural degradation of the sensitive interphases, strict low-dose imaging protocols were utilized. All cryo-TEM images were acquired at 80 K with an low electron dose (~10 $e/Å^2 \cdot s$) using a direct-detect device (Falcon 4). For cryo-EELS mapping, the beam current was maintained at 11 pA with a 0.1 s dwell time per pixel, and the resulting EELS spectra were summed over several adjacent pixels. In addition, control experiments were performed to evaluate possible beam-induced effects. Specifically, under identical imaging conditions but without applying cyclic voltammetry, no lithium precipitation was observed. This comparison ensured that the observed deposition behavior was not an artifact of beam-induced effects.

Surface chemical states were analyzed via XPS (Thermo Scientific K-Alpha) with monochromated Al Kα radiation (1486.6 eV, 150 W), and binding energies were calibrated against the adventitious carbon C 1 s peak at 284.8 eV to ensure charge compensation consistency. For depth profiling in XPS, Ar^+ ions with accelerating voltages of 0.5 keV were applied.

Cell testing

To evaluate the electrochemical performance, CR2025-type coin cells (Guangdong Canrd New Energy Technology Co., Ltd., China) were constructed under an argon atmosphere. In these cells, a pure lithium foil acted as both the counter and reference electrodes with 60 μL of electrolyte. For Li||Cu half cells, Li metal foils (thickness 0.6 mm) were punched into 10 mm discs and the Cu foils were punched into 12 mm discs. For Li||Li symmetric cells, Li metal chips with a diameter of 14 mm were used as electrodes. Tafel plots were generated from LSV results of Li||Li symmetric cells, spanning from −0.2 V to 0.2 V at 1 mV s^{-1}.

Computational details

In this work, all the theoretical calculations have been performed through the molecular dynamic (MD) simulations and density functional theory (DFT) embedded in the Forcite and CASTEP packages, respectively[26]. For MD simulations of different Li electrolytes to unravel the solvation structures, we have chosen the NPT ensemble for all the electrolyte models under 298 K and 1 atm based on fine quality. To achieve the full equilibrium state of the electrolyte, we have performed an annealing process before the MD simulations of 1 ns with each step of 1 fs. The Nosé-Hoover thermostat is the temperature control method for all MD simulations with a Q ratio of 0.1. For the 1 M electrolyte constructions, we have built up the electrolyte system with Li: $TFSI^-/PF_6^-/ClO_4^-$: PC = 20:20:240, for LiTFSI, $LiPF_6$, and $LiClO_4$. For the MD simulations of electrolyte interacting with Li surface, we have

chosen the NVT ensemble for all the electrolyte models under 298 K based on fine quality. The Universal forcefield is applied with fine quality for all the MD simulations. Each simulation step has been set to 1 fs, and the total simulation time is 5 ps with 5000 steps. For the MD simulations, we have constructed electrolyte models, where the Li salt: PC ratio is 1:10 with a random mix on the Li surface (Suppl. Data 1–3). The Li surfaces are cleaved from (100) with 6-layer thickness in a $3 \times 3 \times 1$ supercell. For each electrolyte, we have placed 10 Li salt molecules and 1 PC molecule on the Li surface (Suppl. Data 8–10). For the large electrolyte models, we have cleaved (100) surfaces of Li with 10-layer thickness in a $10 \times 10 \times 1$ supercell consisting of 2000 Li atoms.

Density functional theory (DFT) calculations were performed using the generalized gradient approximation (GGA) with the Perdew–Burke–Ernzerhof (PBE) functional to describe exchange–correlation interactions[27–29]. Meanwhile, the plane-wave basis cutoff energy has been set to 380 eV based on fine quality with the ultrasoft pseudopotentials selection. We have adopted the k-point setting based on coarse quality and the Broyden-Fletcher-Goldfarb-Shannon (BFGS) algorithm is adopted for all the energy minimizations[30]. For all the geometry optimizations in DFT calculations, the convergence should satisfy that the Hellmann-Feynman forces and the total energy difference are smaller than 0.001 eV/Å and 5×10^{-5} eV/atom, respectively. To investigate the interaction of different electrolytes with the Li surface, we have placed 1 Li salt molecules and 4 PC molecules on the surface (Suppl. Data 4–7). In addition, we have introduced 20 Å in the c-axis to guarantee geometry optimizations.

Data availability

All data supporting the findings of this study are available in the paper and its Supplementary Information. Source data are provided with this paper.

References

1. Wu, L.-Q. et al. Unveiling the role of fluorination in hexacyclic coordinated ether electrolytes for high-voltage lithium metal batteries. *J. Am. Chem. Soc.* **146**, 5964–5976 (2024).
2. Xie, Z. et al. Rechargeable alkali metal–chlorine batteries: Advances, challenges, and future perspectives. *Chem. Soc. Rev.* **53**, 8424–8456 (2024).
3. Lu, Y. et al. Breaking the molecular symmetricity of sulfonimide anions for high-performance lithium metal batteries under extreme cycling conditions. *Nat. Energy* **10**, 191–204 (2025).
4. Liang, P. et al. Competitive coordination of ternary anions enabling fast Li-ion desolvation for low-temperature lithium metal batteries. *Adv. Funct. Mater.* **34**, 2309858 (2024).
5. Li, Z. et al. Lithiated metallic molybdenum disulfide nanosheets for high-performance lithium–sulfur batteries. *Nat. Energy* **8**, 84–93 (2023).
6. Liu, J. et al. Optimizing interface concentration and electric fields for enhanced lithium deposition behavior in lithium metal anodes. *Energy Environ. Sci.* **17**, 5993–6002 (2024).
7. Sun, Z. et al. In situ transmission electron microscopy for understanding materials and interfaces challenges in all-solid-state lithium batteries. *eTransportation* **14**, 100203 (2022).
8. Gu, Z. et al. Insights into the anode-initiated and grain boundary-initiated mechanisms for dendrite formation in all-solid-state lithium metal batteries. *Adv. Energy Mater.* **13**, 2302945 (2023).
9. Xie, Y. et al. Dual-protective role of pm475: Bolstering anode and cathode stability in lithium metal batteries. *Adv. Funct. Mater.* **34**, 2310867 (2024).
10. Min, J. et al. Investigating the effect of heterogeneities across the electrode|multiphase polymer electrolyte interfaces in high-potential lithium batteries. *Nat. Nanotechnol.* **20**, 787–797 (2025).
11. Zhou, J. et al. Dual-interphase-stabilizing sulfolane-based electrolytes for high-voltage and high-safety lithium metal batteries. *Adv. Sci.* **11**, 2410129 (2024).
12. Hu, H., Yang, R. & Zeng, Z. Liquid-phase TEM study of electrochemical reactions at multiple interfaces. *Matter* **8**, 101939 (2025).
13. Zhou, S. et al. Visualizing interfacial collective reaction behaviour of Li–S batteries. *Nature* **621**, 75–81 (2023).
14. Lu, X., Hwang, S. & He, K. In situ TEM for structural and chemical evolutions of bimetallic Pt–Ni nanoparticles at elevated temperatures: Implications for heterogeneous catalysis. *ACS Appl. Nano Mater.* **7**, 15735–15742 (2024).
15. Dachraoui, W., Pauer, R., Battaglia, C. & Erni, R. Operando electrochemical liquid cell scanning transmission electron microscopy investigation of the growth and evolution of the mosaic solid electrolyte interphase for lithium-ion batteries. *ACS Nano* **17**, 20434–20444 (2023).
16. Yang, R. et al. Fabrication of liquid cell for in situ transmission electron microscopy of electrochemical processes. *Nat. Protoc.* **18**, 555–578 (2023).
17. Li, Z., Wang, L., Huang, X. & He, X. Lithium bis(trifluoromethanesulfonyl)imide (LiTFSI): A prominent lithium salt in lithium-ion battery electrolytes – fundamentals, progress, and future perspectives. *Adv. Funct. Mater.* **34**, 2408319 (2024).
18. Liu, Y. et al. Self-assembled monolayers direct a LiF-rich interphase toward long-life lithium metal batteries. *Science* **375**, 739–745 (2022).
19. Chen, Y. et al. Origin of dendrite-free lithium deposition in concentrated electrolytes. *Nat. Commun.* **14**, 2655 (2023).
20. Wang, Y. et al. Electroless formation of a fluorinated Li/Na hybrid interphase for robust lithium anodes. *J. Am. Chem. Soc.* **143**, 2829–2837 (2021).
21. Wang, S.-H. et al. Tuning wettability of molten lithium via a chemical strategy for lithium metal anodes. *Nat. Commun.* **10**, 4930 (2019).
22. Chen, C.-C., Fu, L. & Maier, J. Synergistic, ultrafast mass storage and removal in artificial mixed conductors. *Nature* **536**, 159–164 (2016).
23. Sun, X. et al. Epitaxial electrodeposition of lithium metal in cubic Wulff structures. *Angew. Chem. Int. Ed.* **64**, e202506119 (2025).
24. Cai, K. et al. Reconstruction of the solid electrolyte interphase through an in-situ periodic healing strategy in anode-free lithium metal batteries. *ACS Energy Lett.* **6**, 3014–3024 (2025).
25. Chen, Y. et al. Li metal deposition and stripping in a solid-state battery via coble creep. *Nature* **578**, 251–255 (2020).
26. Clark, S. J. et al. First principles methods using castep. *Z. Fur Kristallographie* **220**, 567–570 (2005).
27. Perdew, J. P., Burke, K. & Ernzerhof, M. Generalized gradient approximation made simple. *Phys. Rev. Lett.* **77**, 3865–3868 (1996).
28. Hasnip, P. J. & Pickard, C. J. Electronic energy minimisation with ultrasoft pseudopotentials. *Comput. Phys. Commun.* **174**, 24–29 (2006).
29. Perdew, J. P. et al. Atoms, molecules, solids, and surfaces: Applications of the generalized gradient approximation for exchange and correlation. *Phys. Rev. B* **46**, 6671–6687 (1992).
30. Head, J. D. & Zerner, M. C. A Broyden—Fletcher—Goldfarb—shanno optimization procedure for molecular geometries. *Chem. Phys. Lett.* **122**, 264–270, (1985).

Author contributions

Z. Zeng conceived and guided the project. H. Hu designed and performed the experiments. G. Fang, H. Liao, D. Chao, So. Kim and J. Lee helped to analyze the results. M. Sun and B. Huang conducted the DFT calculations and MD simulations. Z. Zhang and M. Gu performed the cryo-STEM test of the samples. H. Hu, M. Sun, Se. Kim, X. Yang, L. Mei, R. Yan, W. Zheng, Y. Zhang, J. Li, and Z. Zeng drafted the paper. All authors checked the paper and agreed with its content.

Funding
Z. Zeng discloses support for the research of this work from Hong Kong RGC's Young Collaborative Research Grant [grant number C1003-23Y], General Research Fund [grant numbers 11308923, 11309824, and 11309425], City University of Hong Kong's internal grant [grant numbers 7005462 and 7005623] and Hong Kong ITC's ITF project [grant number ITS/192/23].

Competing interests
The authors declare no competing interests.

Additional information
Supplementary information The online version contains supplementary material available at https://doi.org/10.1038/s41467-026-74340-1.

Correspondence and requests for materials should be addressed to M. Danny Gu, Bolong Huang, Ju Li or Zhiyuan Zeng.

Peer review information *Nature Communications* thanks Zeyi Wang and the other anonymous reviewer(s) for their contribution to the peer review of this work. A peer review file is available.

[1]Department of Materials Science and Engineering, State Key Laboratory of Marine Environmental Health, City University of Hong Kong, Hong Kong, China. [2]Eastern Institute for Advanced Study, Eastern Institute of Technology, Zhejiang, People's Republic of China. [3]Department of Chemistry, City University of Hong Kong, Hong Kong, China. [4]Department of Nuclear Science and Engineering, Massachusetts Institute of Technology, Cambridge, MA, USA. [5]Department of Mechanical Engineering, Yonsei University, Seoul, Republic of Korea. [6]School of Materials Science and Engineering, Key Laboratory of Electronic Packaging and Advanced Functional Materials of Hunan Province, Central South University, Changsha, PR China. [7]Laboratory of Advanced Materials, Shanghai Key Laboratory of Molecular Catalysis and Innovative Materials, Fudan University, Shanghai, China. [8]State Key Lab of Physical Chemistry of Solid Surfaces, College of Chemistry and Chemical Engineering, Xiamen University, Xiamen, China. [9]Shenzhen Research Institute, City University of Hong Kong, Shenzhen, China. [10]These authors contributed equally: Honglu Hu, Zhen Zhang, Mingzi Sun. ✉e-mail: m.danny.gu@gmail.com; b.h@cityu.edu.hk; liju@mit.edu; zhiyzeng@cityu.edu.hk

Supporting Information

Operando identification of anion effect on lithium nucleation and growth via *in situ* transmission electron microscopy

Honglu Hu[1,#], Zhen Zhang[2,#], Mingzi Sun[3,#], So Yeon Kim[4], Se Young Kim[5], Xinru Yang[1], Liang Mei[1], Ruixin Yan[1], Weikang Zheng[1], Yue Zhang[1], M. Danny Gu[2]*, Guozhao Fang[6], Dongliang Chao[7], Hong-Gang Liao[8], Joon Sang Lee[5], Bolong Huang[3]*, Ju Li[4]*, Zhiyuan Zeng[1,9]*

[1] Department of Materials Science and Engineering, State Key Laboratory of Marine Environmental Health, City University of Hong Kong, Hong Kong 999077, China

[2] Eastern Institute for Advanced Study, Eastern Institute of Technology, Ningbo, Zhejiang, People's Republic of China

[3] Department of Chemistry, City University of Hong Kong, Hong Kong, People's Republic of China

[4] Department of Nuclear Science and Engineering and Department of Materials Science and Engineering, Massachusetts Institute of Technology, Cambridge, MA, USA

[5] Department of Mechanical Engineering, Yonsei University, 50 Yonsei-ro, Seodaemun-gu, Seoul, Republic of Korea

[6] School of Materials Science and Engineering, Key Laboratory of Electronic Packaging and Advanced Functional Materials of Hunan Province, Central South University, Changsha, PR China

[7] Laboratory of Advanced Materials, Aqueous Battery Center, Shanghai Key Laboratory of Molecular Catalysis and Innovative Materials, Faculty of Chemistry and Materials, Fudan University, Shanghai, China

[8] State Key Lab of Physical Chemistry of Solid Surfaces, College of Chemistry and Chemical Engineering, Xiamen University, Xiamen, People's Republic of China

[9] Shenzhen Research Institute, City University of Hong Kong, Shenzhen, People's Republic of China

[#] These authors contributed equally.

* Corresponding authors: Zhiyuan Zeng, Ju Li, Bolong Huang, M. Danny Gu.

Contents

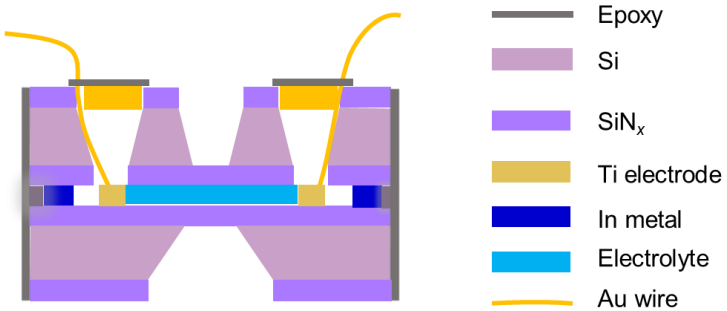

Supplementary Fig. 1. | Schematic illustration of an electrochemical liquid cell from the cross-sectional views. The liquid cell features a layered architecture comprising silicon substrates with patterned silicon nitride (SiN_x) imaging windows, fabricated through sequential lithography and etching processes. Between the top and bottom chips, a precisely defined microfluidic chamber contains deposited titanium electrodes for electrochemical control, formed by physical vapor deposition and aligned through thermal compression bonding. The chamber is encapsulated with epoxy sealing and filled with liquid electrolyte via capillary action, while copper foil covers the reservoirs to prevent leakage. The final assembly integrates indium spacers for structural stability and wire-bonded connections for electrical interfacing, enabling in situ TEM observation of electrochemical processes through the ultrathin SiN_x membrane.

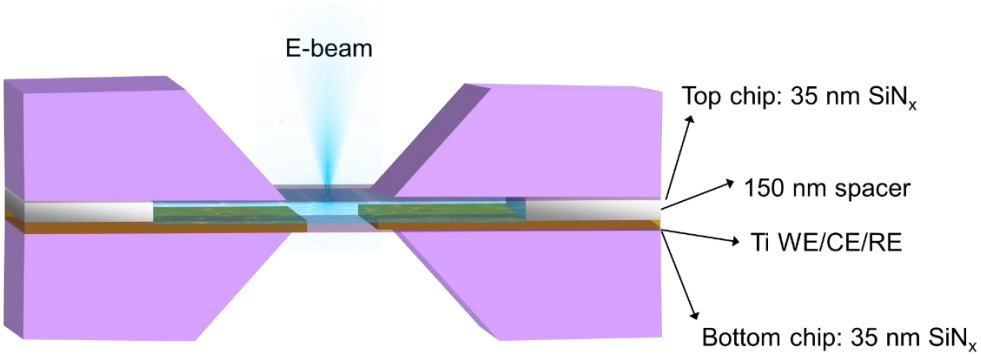

Supplementary Fig. 2. | Schematic illustration of an electrochemical liquid cell composed of top/bottom chips with 35-nm SiN_x observation windows, 150-nm spacers and Ti electrodes in electrolytes.

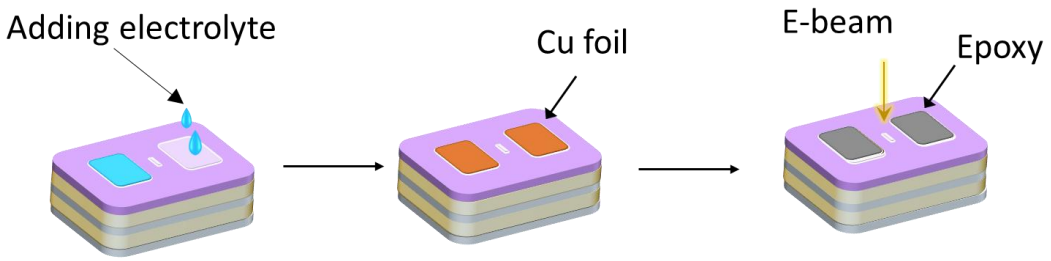

Supplementary Fig. 3. | The liquid-cell fabrication schematic illustrates the preparation steps conducted within an argon-filled glovebox. Following cell assembly, electrolytes containing different Li salts were introduced into the cell through capillary action, after which the system was hermetically sealed using epoxy.

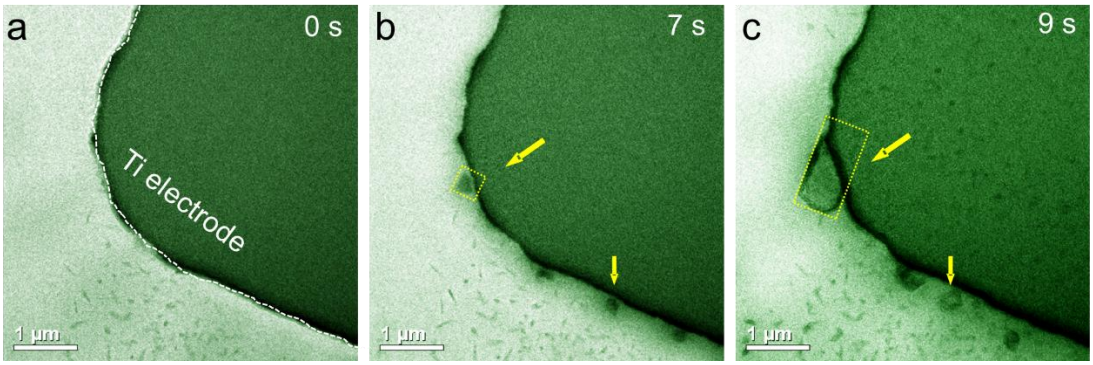

Supplementary Fig. 4. | Parallelogram shaped Li deposition at the edge of Ti electrode in $LiClO_4$-PC electrolyte. **a**, Initial state without charge, **b**, Li nucleation and **c**, Li growth. (Supplementary Video 4).

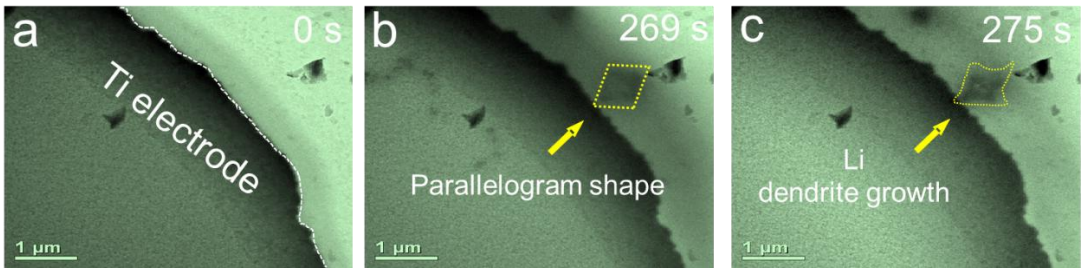

Supplementary Fig. 5. | Deposition and dendrite growth of parallelogram shaped Li at the edge of Ti electrode in $LiClO_4$-PC electrolyte. **a**, Initial state without charge, **b**, Parallelogram shape Li growth and **c**, Li dendrite growth. (Supplementary Video 5).

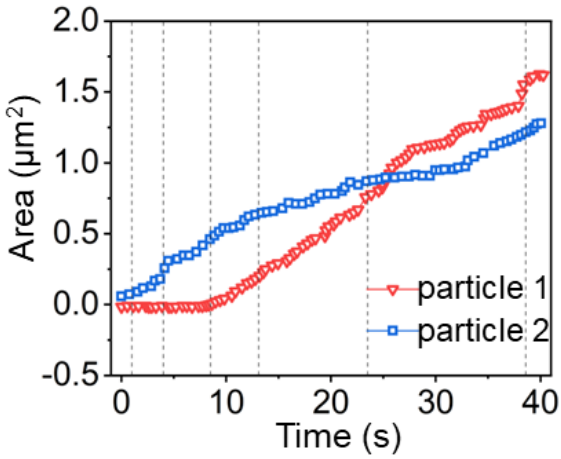

Supplementary Fig. 6. | The corresponding projection area variation as a function of time of particles 1 and 2 in Fig. 2a. Source data are provided as a Source Data file.

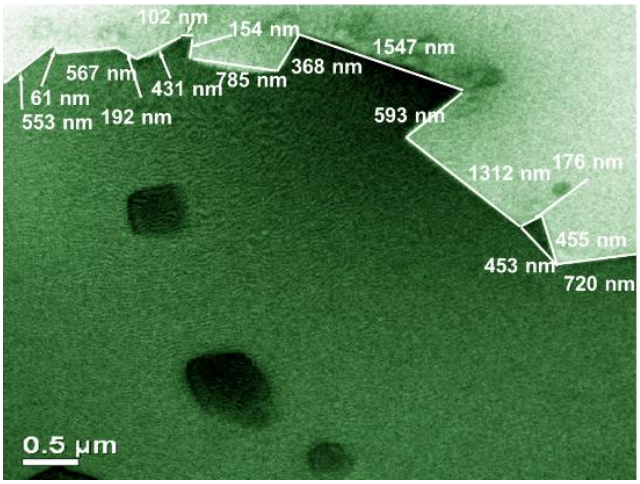

Supplementary Fig. 7. | Ti electrode size details for $LiPF_6$-PC electrolyte.

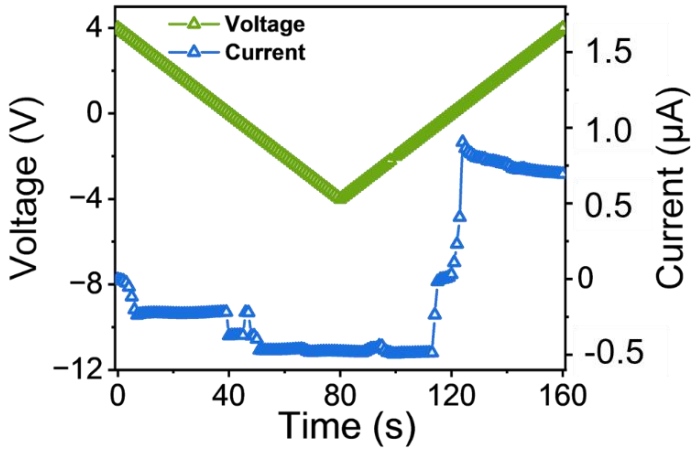

Supplementary Fig. 8. | Voltage loaded on the electrochemical liquid cell with LiTFSI-PC electrolyte and measured current from electrochemical workstation (Corresponding to Supplementary Video 3). Electrochemical tests were conducted at 20 °C. Source data are provided as a Source Data file.

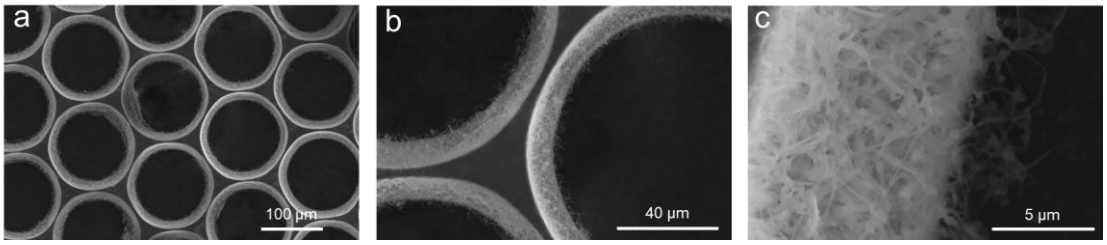

Supplementary Fig. 9. | SEM images for Li metal deposited on bare Cu grid in $LiClO_4$-PC electrolytes at different magnifications of (**a**) 800 times; (**b**) 3000 times and (**c**) 24000 times. Batteries for SEM tests were in a fully discharged state after 3-cycle cycling at 20 °C with a current density of 2.0 mA cm^{-2} and a capacity density of 1.0 mAh cm^{-2}.

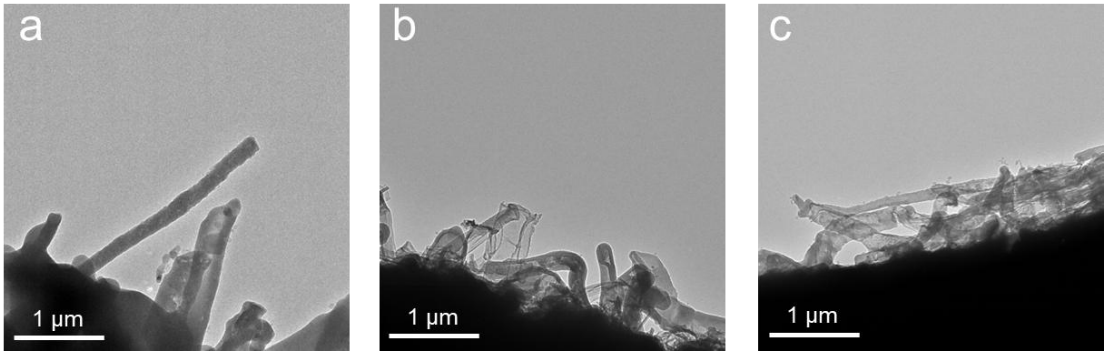

Supplementary Fig. 10. | Low magnification Cryo-TEM images. Cryo-TEM images of deposited Li in different electrolytes: (**a**) $LiClO_4$-PC; (**b**) $LiPF_6$-PC; (**c**) LiTFSI-PC. The current density is 2.0 mA cm^{-2}, and the capacity is 1.0 mAh cm^{-2}.

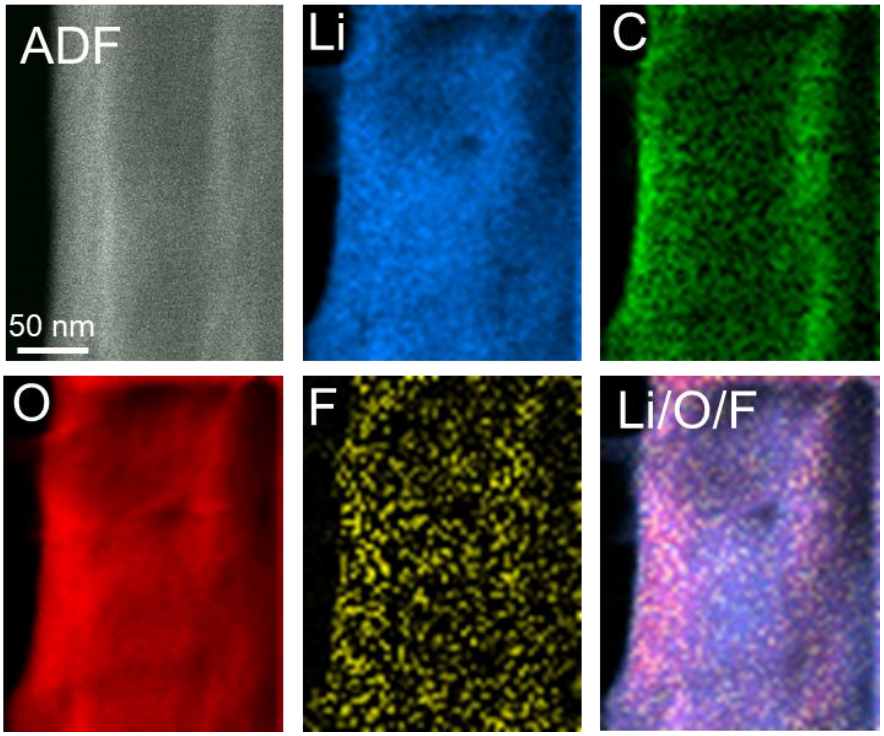

Supplementary Fig. 11. | Cryo-STEM ADF images and EELS mapping images of SEI on Li metal in the $LiPF_6$ electrolytes after thirty charging/discharging cycles in Li/Cu cells. Batteries for cryo-STEM tests were in a fully discharged state after 30-cycle cycling at 20 °C with a current density of 2.0 mA cm^{-2} and a capacity density of 1.0 mAh cm^{-2}.

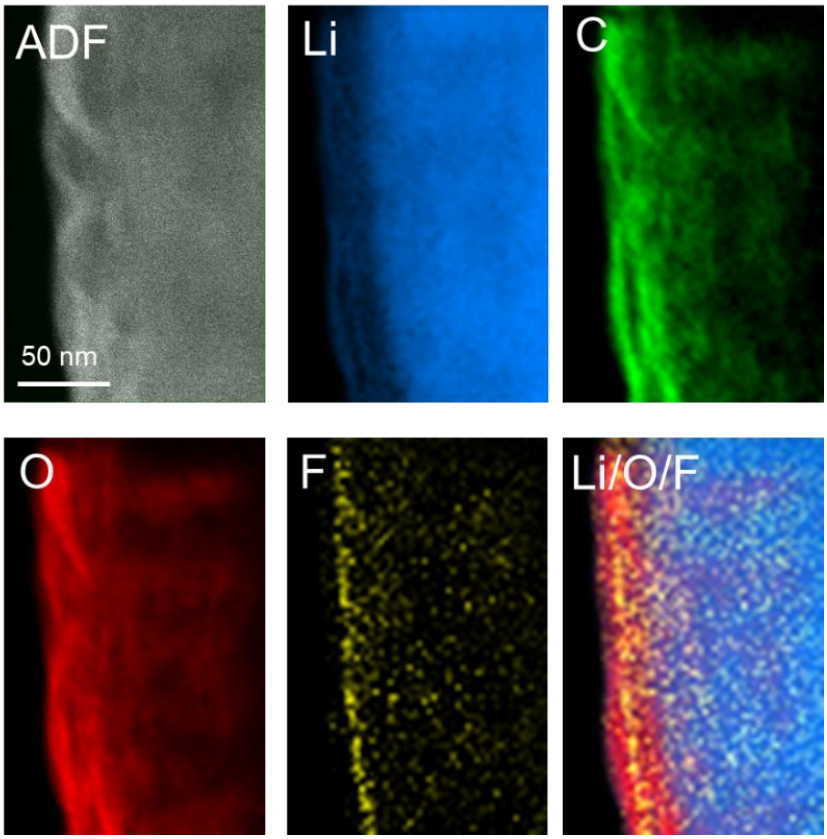

Supplementary Fig. 12. | Cryo-STEM ADF images and EELS mapping images of SEI on Li metal in the LiTFSI electrolytes after thirty charging/discharging cycles in Li/Cu cells. Batteries for cryo-STEM tests were in a fully discharged state after 30-cycle cycling at 20 °C with a current density of 2.0 mA cm^{-2} and a capacity density of 1.0 mAh cm^{-2}.

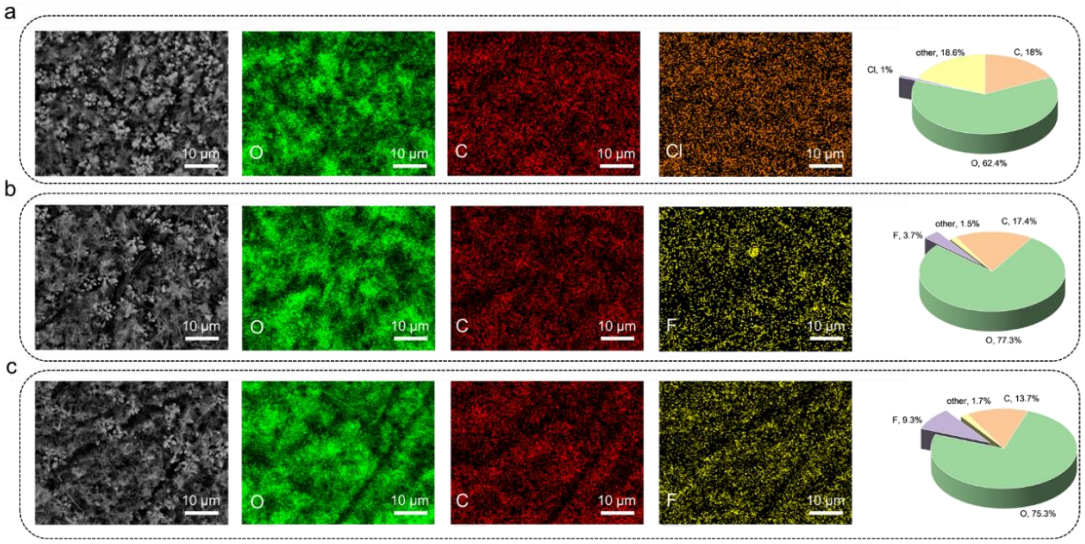

113

114 **Supplementary Fig. 13.** | SEM images of Elemental O, C, Cl, and F mapping and

115 content proportion (wt. %) of the Li surface deposited in in $LiClO_4$ (**a**), $LiPF_6$ (**b**) and

116 LiTFSI (**c**) electrolytes. Batteries for SEM tests were in a fully discharged state after 3-

117 cycle cycling at 20 °C with a current density of 2.0 mA cm^{-2} and a capacity density of

118 1.0 mAh cm^{-2}.

119

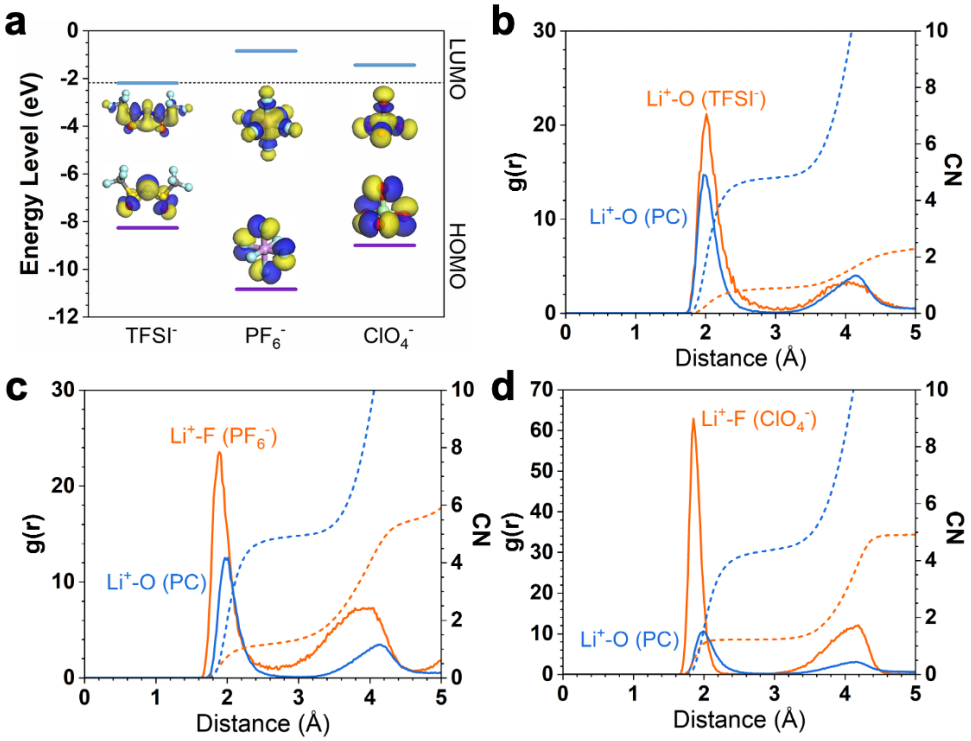

Supplementary Fig. 14. | **a**, The HOMO/LUMO orbitals of different anions. The RDF and CN of (**b**) 1M LiTFSI, (**c**) $LiPF_6$, and (**d**) $LiClO_4$. Source data are provided as a Source Data file.

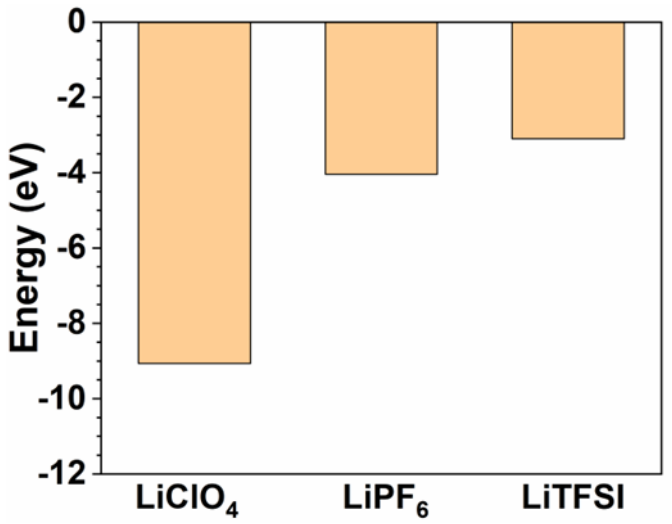

Supplementary Fig. 15. | The interaction energies of different electrolytes with the Li surface. Source data are provided as a Source Data file.

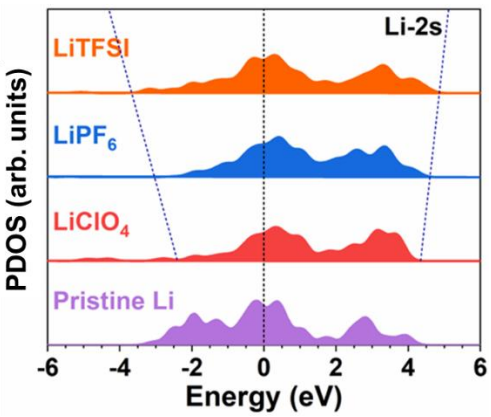

Supplementary Fig. 16. | The PDOSs of Li-2s orbitals of surface Li after adsorption of electrolyte molecules. Source data are provided as a Source Data file.

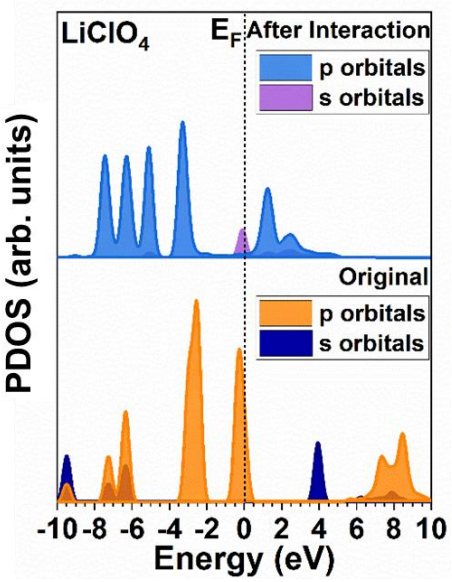

141

142 **Supplementary Fig. 17. |** The PDOS comparisons of electrolyte molecules in $LiClO_4$

143 electrolyte. Source data are provided as a Source Data file.

144

145

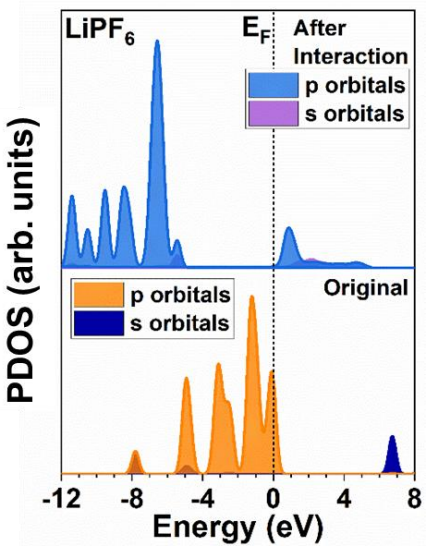

146

147 **Supplementary Fig. 18. |** The PDOS comparisons of electrolyte molecules in $LiPF_6$

148 electrolyte. Source data are provided as a Source Data file.

149

150

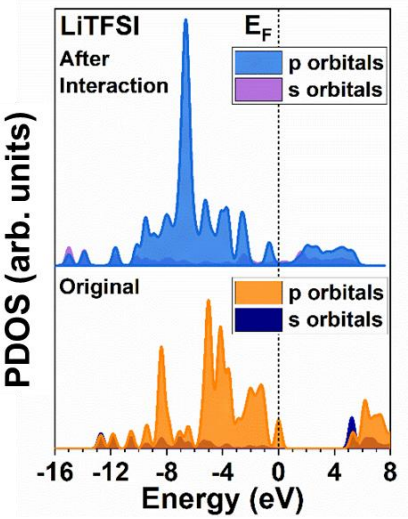

Supplementary Fig. 19. | The PDOS comparisons of electrolyte molecules in LiTFSI electrolyte. Source data are provided as a Source Data file.

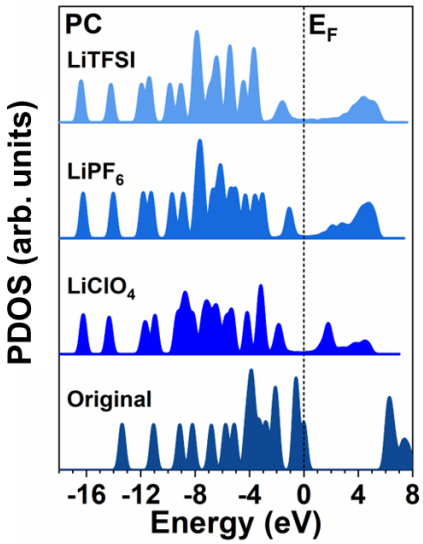

157

158 **Supplementary Fig. 20. |** The PDOSs of Li-2s orbitals of surface Li after adsorption

159 of electrolyte molecules. Source data are provided as a Source Data file.

160

161

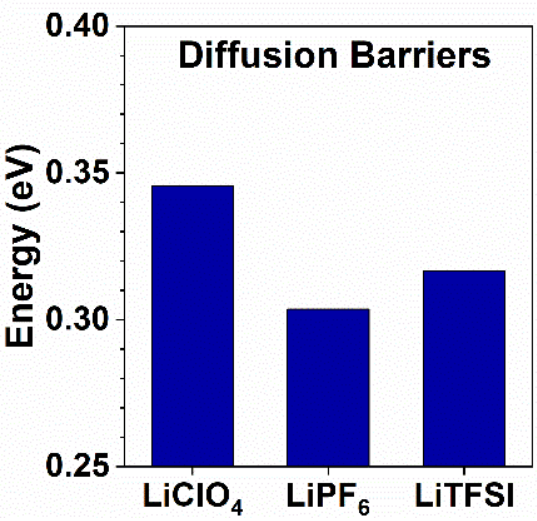

Supplementary Fig. 21. | The Li diffusion barriers on the surface with different electrolytes. Source data are provided as a Source Data file.

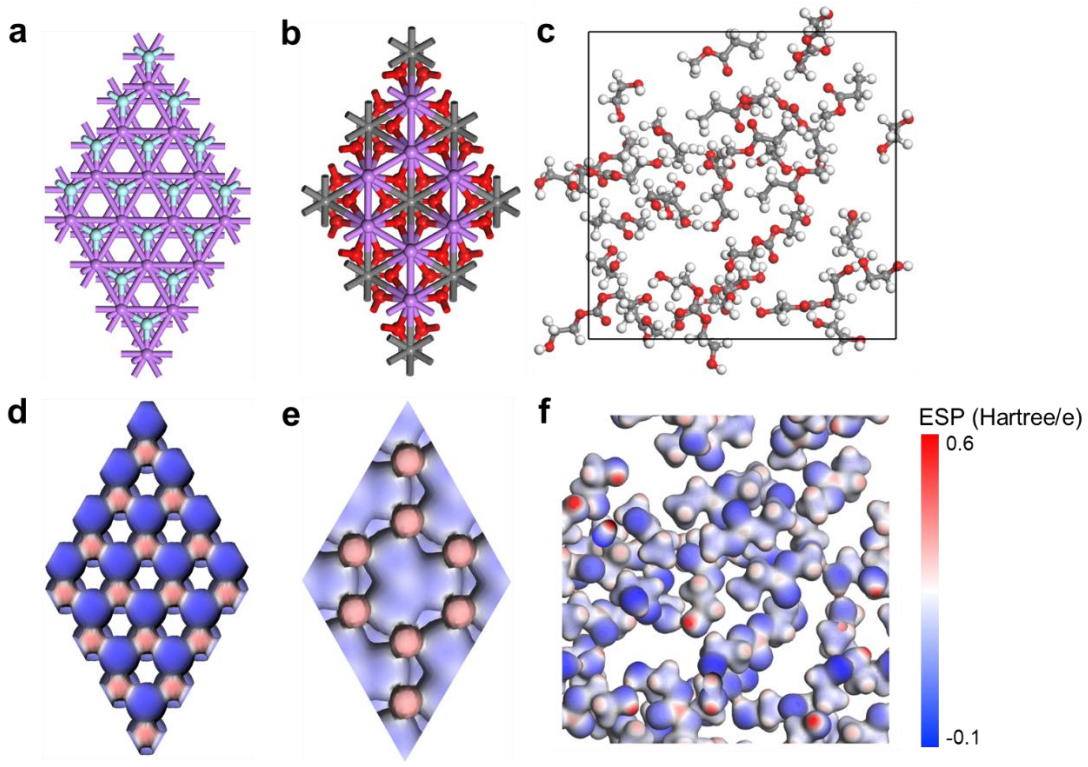

Supplementary Fig. 22. | The lattice structure of the SEI layer: (**a**) LiF (001), (**b**) Li_2CO_3 (001), and (**c**) amorphous organic phase. The electrostatic potential of (**d**) LiF (001), (**e**) Li_2CO_3 (001), and (**f**) amorphous organic phase.

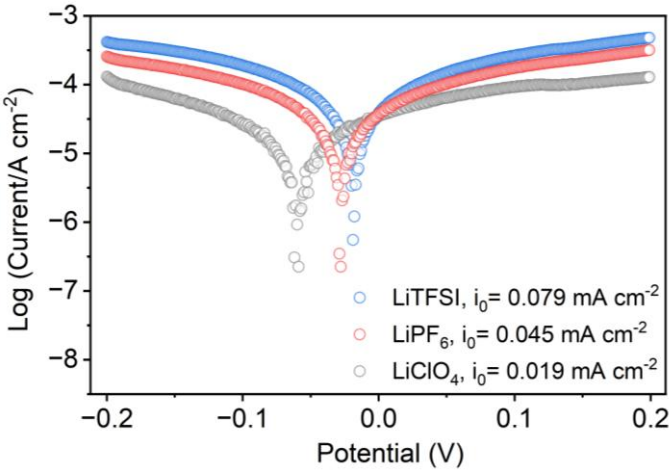

Supplementary Fig. 23. | Tafel plots and exchange current densities of different electrolytes. Tafel curves derived from Li||Li symmetric cells using 1 M $LiClO_4$-PC, 1 M $LiPF_6$-PC, and 1 M LiTFSI-PC electrolytes, respectively. The corresponding exchange current densities (i_0) are calculated by fitting the linear polarization regions, yielding 0.0.019, 0.045, and 0.079 mA cm^{-2}, respectively. All electrochemical tests were conducted at 20 °C. Source data are provided as a Source Data file.

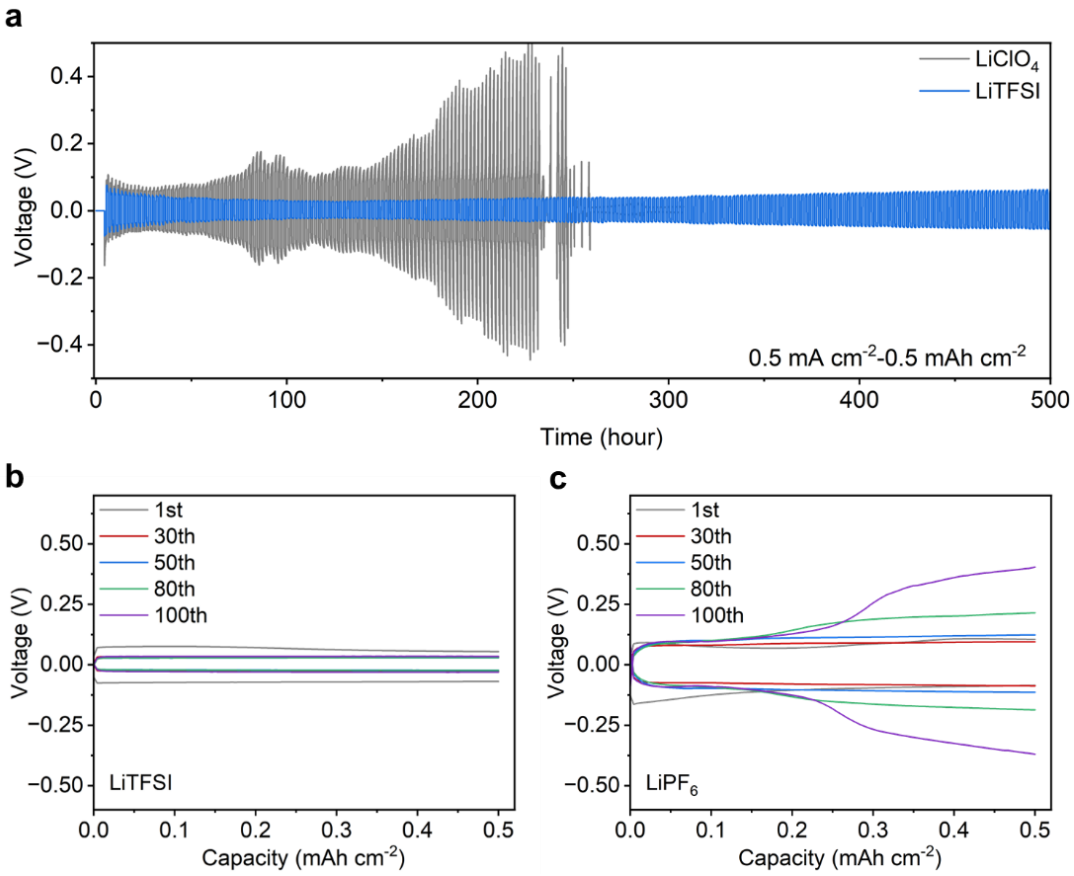

181

182 **Supplementary Fig. 24.** | Long-term cycling test of Li||Li symmetric cells (**a**) and

183 voltage-capacity curves of batteries cycled in 1 M LiTFSI-PC (**b**) and 1 M $LiClO_4$-PC

184 (**c**) electrolytes at a current density of 0.5 mA cm^{-2} with a capacity of 0.5 mAh cm^{-2}.

185 All electrochemical tests were conducted at 20 °C. Source data are provided as a Source

186 Data file.

187

188

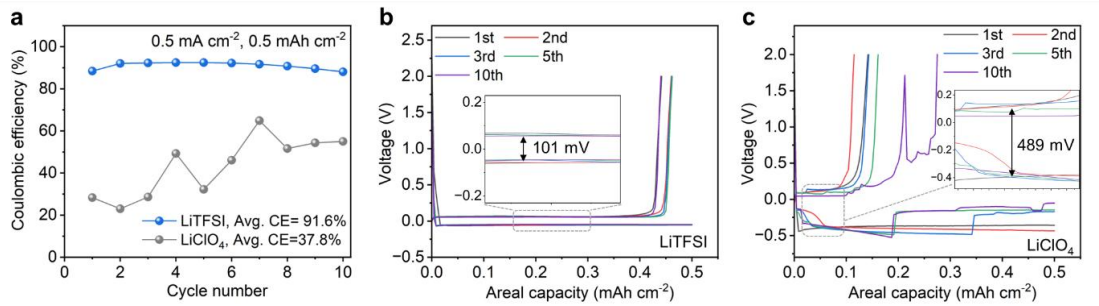

Supplementary Fig. 25. | Coulombic efficiency (CE) of Li||Cu half-cells within the first 10 cycles (**a**) and voltage-areal capacity curves of batteries cycled in 1 M LiTFSI-PC (**b**) and 1 M $LiClO_4$-PC (**c**) electrolytes at 0.5 mA cm^{-2} and 0.5 mAh cm^{-2}. All electrochemical tests were conducted at 20 °C. Source data are provided as a Source Data file.

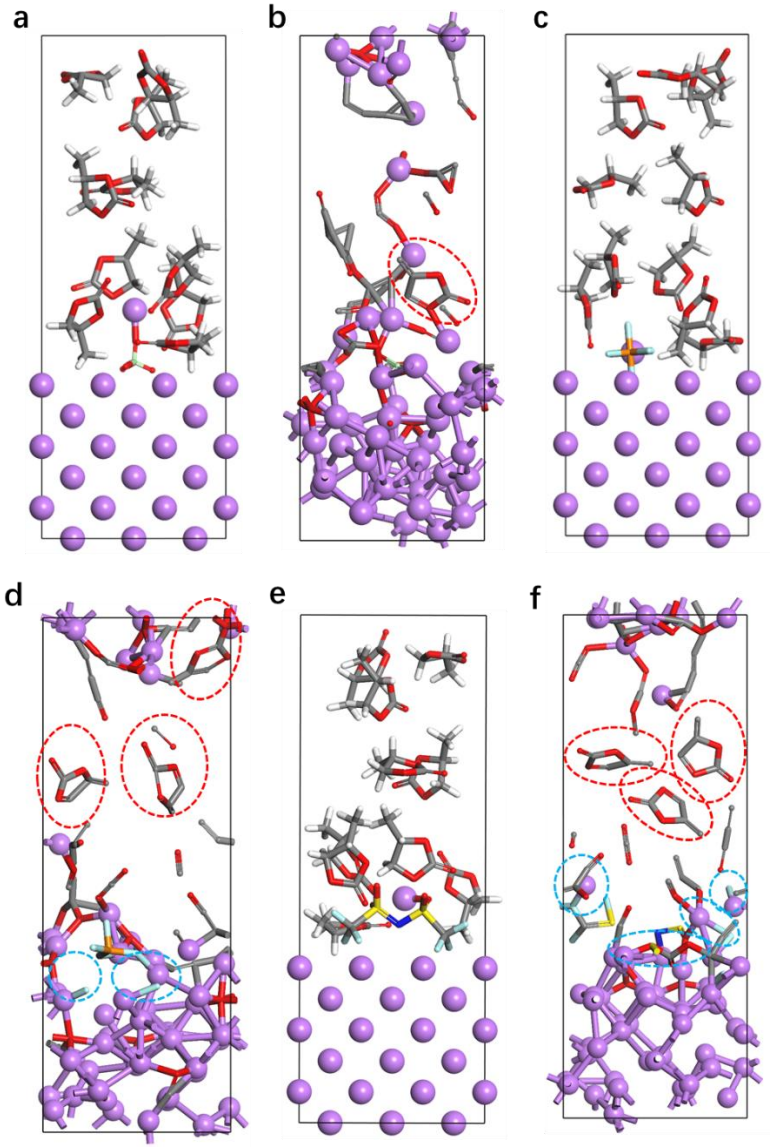

Supplementary Fig. 26. | Theoretical calculation of Li decomposition in different electrolytes. The electrolyte structure with PC: Electrolyte = 10:1 before MD simulations of (**a**) $LiClO_4$, (**c**) $LiPF_6$, and (**e**) LiTFSI electrolytes. The electrolyte structure with PC: Electrolyte = 10:1 after MD simulations of (**b**) $LiClO_4$, (**d**) $LiPF_6$, and (**f**) LiTFSI electrolytes. Red circles indicate the PC without decomposition. Blue circles indicate the formation of other molecules including LiF and Li_2CO_3. Purple balls = Li, Green sticks = Cl, Orange sticks = P, Light Blue sticks = F, Yellow sticks = S, Blue sticks = N, Red sticks = O, Green sticks = C and White sticks = H. The H atoms

have not been shown in figures after simulations for better demonstrations. d-f, The PDOS comparisons of electrolyte molecules (**d**) $LiClO_4$, (**e**) $LiPF_6$, and (**f**) LiTFSI. i, The PDOS changes of PC in different electrolytes after interactions with the Li surface. k, The PDOSs of Li-2s orbitals of surface Li after adsorption of electrolyte molecules.

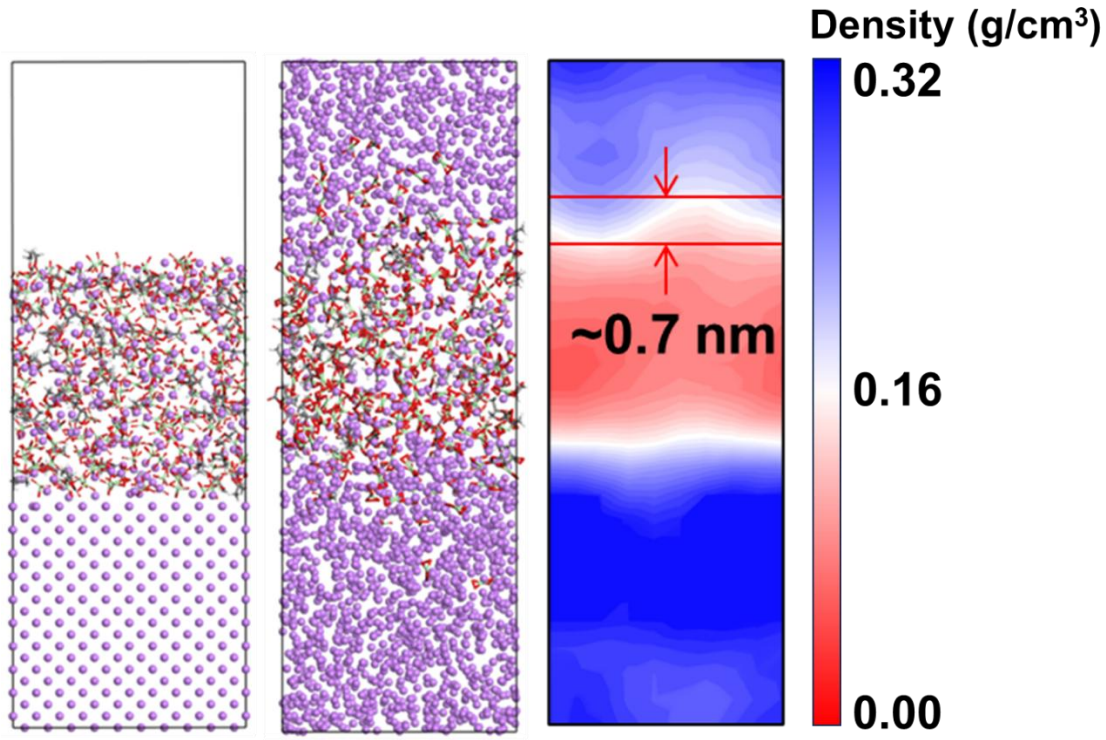

Supplementary Fig. 27. | The MD simulations of $LiClO_4$ electrolyte on a 10×10×10 supercell of Li surface before MD simulations. Left panel: before MD simulations. Middle: after MD simulations. Right: The density mapping of Li ions after MD simulations. Color bar: Purple = Li, green = Cl, cyan = F, orange = P, blue = N, yellow = S, red = O, and white = H.

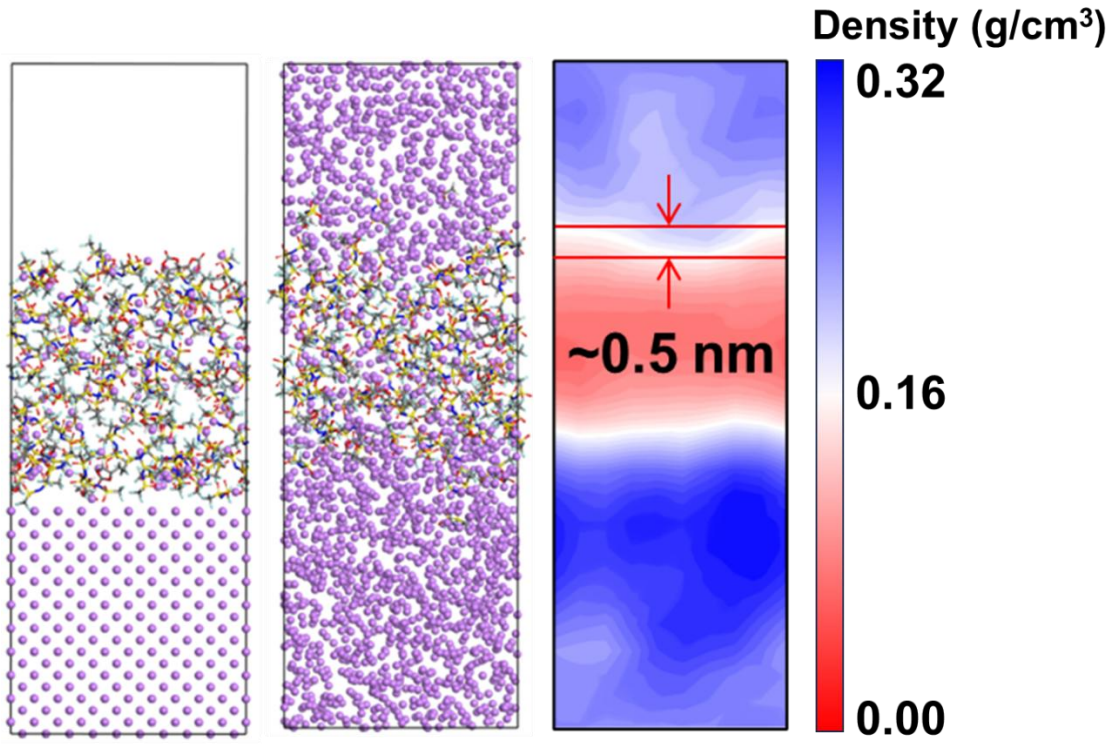

Supplementary Fig. 28. | The MD simulations of LiTFSI electrolyte on a 10×10×10 supercell of Li surface before MD simulations. Left panel: before MD simulations. Middle: after MD simulations. Right: The density mapping of Li ions after MD simulations. Color bar: Purple = Li, green = Cl, cyan = F, orange = P, blue = N, yellow = S, red = O, and white = H.

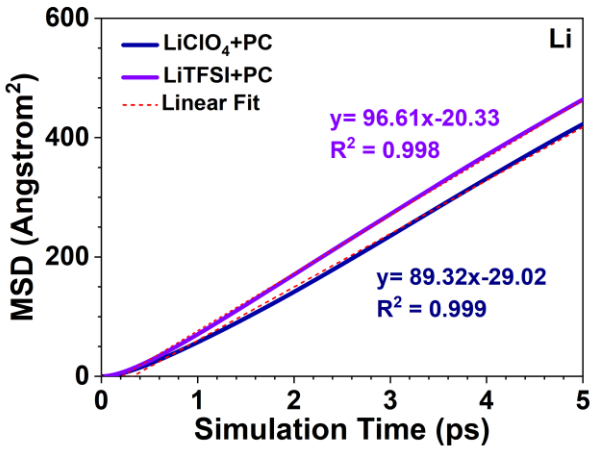

225

226 **Supplementary Fig. 29. |** The MSD of electrolytes after MD simulations. Source data

227 are provided as a Source Data file.

228

Supplementary Table S1. | Comparisons between commercial liquid cells with our design in this work.

Key parameters	DENS solutions[1-3]	Hummingbird Scientific[4]	Protochips[5-7]	This work
Thickness of SiN_x window	~50 nm	~50 nm	~50 nm	~35 nm
Thickness of liquid layer	~200 or ~500 nm	~1000 nm	~500 or ~1000 nm	~150 nm
TEM spatial resolution	~50 nm	~100 nm	~100 nm	~15 nm

Supplementary Table S2. | Representative mechanical properties of primary SEI components.

SEI Component	Chemical nature	Young's Modulus (*E*, GPa)
LiF	Inorganic	~ 65.0 – 149.0 [8]
Li_2CO_3	Inorganic	~ 45.0 – 70.0 [9]
Li_2O	Inorganic	> 60 [10]
Organics (e.g., $ROCO_2Li$, oligomers)	Organic	< 5.0 [10,11]

Supplementary Table S3. |A comparison of LP-TEM cell configurations in recent representative studies.

Focus of LP-TEM Study	Thickness of SiN_x window (nm)	Thickness of liquid layer (nm)	Microchips maker	Reference
SEI dynamics & Li deposition	10	100	Custom	Zhou et al.[12]
Li nucleation & growth	50	150	Custom	Walid et al.[13]
Li anode reversibility	50	500	Commercial (Protochips)	Hayoung et al.[14]
Zn dendrite formation	N.A.	150	Custom	Seung et al.[15]
Li/O_2 batteries	50	500	N.A.	Lee et al.[16]
Zn dendrite formation	15	100	Custom	Zeng et al.[17]
Na metal batteries	50	500	Commercial (Protochips)	Gong et al.[18]
Operando Li nucleatio imaging	35	150	Custom	This work

Supplementary References

1 Körner, A., Fritsch, B., Morales, A. L., Malgaretti, P. & Hutzler, A. Panta rhei - tuning silver nanostructure evolution with flow and radiolysis in liquid phase STEM. *Nano Today* **61**, 102575, (2025).

2 Arenas Esteban, D. *et al.* Quantitative 3D structural analysis of small colloidal assemblies under native conditions by liquid-cell fast electron tomography. *Nat. Commun.* **15**, 6399, (2024).

3 Park, J. *et al.* Toward quantitative electrodeposition via in situ liquid phase transmission electron microscopy: Studying electroplated zinc using basic image processing and 4D STEM. *Small Methods* **8**, 2400081, (2024).

4 Karki, K., Mefford, T., Alsem, D. H., Salmon, N. & Chueh, W. C. Replicating bulk electrochemistry in liquid cell microscopy. *Microsc. Microanal.* **24**, 324-325, (2018).

5 Gallegos-Moncayo, K. *et al.* Coupling liquid electrochemical TEM and mass-spectrometry to investigate electrochemical reactions occurring in a Na-ion battery anode. *Small Methods* **8**, 2400365, (2024).

6 Parlinska-Wojtan, M. *et al.* Understanding the growth of electrodeposited ptni nanoparticle films using correlated in situ liquid cell transmission electron microscopy and synchrotron radiation. *Nano Lett.* **24**, 12361-12367, (2024).

7 Korpanty, J., Wang, C. & Gianneschi, N. C. Upper critical solution temperature polymer assemblies via variable temperature liquid phase transmission electron microscopy and liquid resonant soft X-ray scattering. *Nat. Commun.* **14**, 3441, (2023).

8 Wang, Y. *et al.* Electroless formation of a fluorinated Li/Na hybrid interphase for

262 robust lithium anodes. *J. Am. Chem. Soc.* **143**, 2829-2837, (2021).

263 9 Wang, X. *et al.* Colloid electrolyte with changed Li^+ solvation structure for high-
264 power, low-temperature lithium-ion batteries. *Adv. Mater.* **35**, 2209140, (2023).

265 10 Wang, A., Kadam, S., Li, H., Shi, S. & Qi, Y. Review on modeling of the anode
266 solid electrolyte interphase (SEI) for lithium-ion batteries. *npj Computational Materials*
267 **4**, 15, (2018).

268 11 Zheng, J. *et al.* 3D visualization of inhomogeneous multi-layered structure and
269 young's modulus of the solid electrolyte interphase (SEI) on silicon anodes for lithium
270 ion batteries. *Phys. Chem. Chem. Phys.* **16**, 13229-13238, (2014).

271 12 Zhou, S. *et al.* Visualizing interfacial collective reaction behaviour of Li–S batteries.
272 *Nature* **621**, 75-81, (2023).

273 13 Dachraoui, W., Pauer, R., Battaglia, C. & Erni, R. Operando electrochemical liquid
274 cell scanning transmission electron microscopy investigation of the growth and
275 evolution of the mosaic solid electrolyte interphase for lithium-ion batteries. *ACS Nano*
276 **17**, 20434-20444, (2023).

277 14 Park, H. *et al.* Early stage Li plating by liquid phase and cryogenic transmission
278 electron microscopy. *ACS Energy Lett.* **8**, 715-721, (2023).

279 15 Lee, S.-Y. *et al.* Lithium metal stripping mechanisms revealed through
280 electrochemical liquid cell electron microscopy. *Nano Energy* **102**, 107641, (2022).

281 16 Lee, D. *et al.* Direct observation of redox mediator-assisted solution-phase
282 discharging of $Li–O_2$ battery by liquid-phase transmission electron microscopy. *J. Am.*
283 *Chem. Soc.* **141**, 8047-8052, (2019).

17 Zeng, H. *et al.* Shape-controlled Zn nanosheet electrodeposition revealed by in situ liquid-phase transmission electron microscopy. *J. Phys. Chem. C* **127**, 22992-22999, (2023).

18 Gong, C. *et al.* Revealing the role of fluoride-rich battery electrode interphases by operando transmission electron microscopy. *Adv. Energy Mater.* **11**, 2003118, (2021).

Description of Additional Supplementary Files

Supplementary Video 1: In situ observation of lithium dendritic growth in $LiClO_4$-PC electrolyte. This video shows the real-time evolution of lithium nucleation and rapid dendritic propagation on a Ti working electrode in a 1 M $LiClO_4$ in propylene carbonate (PC) electrolyte. The footage captures the transition from initial parallelogram-shaped nuclei to anisotropic dendrites.

Supplementary Video 2: In situ observation of mossy lithium growth in $LiPF_6$-PC electrolyte. Real-time tracking of lithium deposition in a 1 M $LiPF_6$ in PC electrolyte. The video demonstrates the synchronized formation of mossy lithium deposits with uniform morphological features and their subsequent reversible dissolution without dendrite formation.

Supplementary Video 3: In situ observation of lithium lateral growth and fusion in LiTFSI-PC electrolyte. This video captures the unique terrace-like nucleation and lateral coalescence of lithium nuclei in a 1 M LiTFSI in PC electrolyte. It highlights the planar expansion and complete reversible dissolution of lithium, characteristic of the TFSI-mediated bilayer interphase.

Supplementary Video 4: Parallelogram-shaped Li nucleation and early deposition at the electrode edge. This video shows the initial state, subsequent Li nucleation, and early growth of parallelogram-shaped Li at the edge of the Ti electrode in the $LiClO_4$-PC electrolyte. It illustrates the severe localized potential fluctuations inherent to $LiClO_4$-based systems.

Supplementary Video 5: Deposition and severe dendritic growth of Li at the electrode edge. This video captures the progression from parallelogram-shaped Li growth to severe Li

dendrite formation at the Ti electrode edge in the $LiClO_4$-PC electrolyte. It further demonstrates the enhanced dendritic growth kinetics in $LiClO_4$-based systems.

Supplementary Data Legends (Computational Files)

Supplementary Data 1: Electrolyte model files for MD calculations. This folder contains the initial and final structural configurations (.cif format) of MD calculations to investigate the solvation structures of $LiClO_4$ electrolytes.

Supplementary Data 2: Electrolyte model files for MD calculations. This folder contains the initial and final structural configurations (.cif format) of MD calculations to investigate the solvation structures of $LiPF_6$ electrolytes.

Supplementary Data 3: Electrolyte model files for MD calculations. This folder contains the initial and final structural configurations (.cif format) of MD calculations to investigate the solvation structures of LiTFSI electrolytes.

Supplementary Data 4: The geometry optimized model files for DFT calculations. This folder contains the optimized geometry (.cif format) for DFT calculations performed to investigate the adsorption energy of $LiClO_4$ on the Li (100) surface.

Supplementary Data 5: The geometry optimized model files for DFT calculations. This folder contains the optimized geometry (.cif format) for DFT calculations performed to investigate the adsorption energy of $LiPF_6$ on the Li (100) surface.

Supplementary Data 6: The geometry optimized model files for DFT calculations. This folder contains the optimized geometry (.cif format) for DFT calculations performed to investigate the adsorption energy of LiTFSI on the Li (100) surface.

Supplementary Data 7: The geometry optimized model files for DFT calculations. This folder contains the optimized geometry (.cif format) for DFT calculations performed to investigate the adsorption energy of PC on the Li (100) surface.

Supplementary Data 8: Electrolyte model files for MD calculations. This folder contains the initial and final structures (.cif format) of MD calculations to investigate the SEI components of $LiClO_4$ electrolytes on the Li (100) surface.

Supplementary Data 9: Electrolyte model files for MD calculations. This folder contains the initial and final structures (.cif format) of MD calculations to investigate the SEI components of $LiPF_6$ electrolytes on the Li (100) surface.

Supplementary Data 10: Electrolyte model files for MD calculations. This folder contains the initial and final structures (.cif format) of MD calculations to investigate the SEI components of LiTSFI electrolytes on the Li (100) surface.